Title

Structural insights into inhibition mechanism of the helicase-primase complex from human herpesvirus 1

Author list

Ko Sato[1], Hisashi Ishida[2], Toma Miyagishi[3], Shunsuke Kobayashi[1], Yoshiaki Kise[4], Keisuke Hamada[1], Chikako Okada[1], Asako Oguni[1], Osamu Nureki[4], Hidetoshi Kono[2], Kaori Fukuzawa[3], Toru Sengoku[1,5]

Affiliations

[1]Department of Biochemistry, Yokohama City University Graduate School of Medicine, 3-9 Fukuura, Kanazawa-Ku, Yokohama, Kanagawa 236-0004, Japan

[2]Insitute for Quantum Life Science, National Institutes for Quantum Science and Technology, 4-9-1 Anagawa, Inage-ku, Chiba, Chiba 263-8555, Japan

[3]Graduate School of Pharmaceutical Sciences, The University of Osaka, 1-6 YamadaOka, Suita, Osaka 565-0871, Japan

[4]Department of Biological Sciences, Graduate School of Science, The University of Tokyo, 7-3-1 Hongo, Bunkyo-ku, Tokyo 113-0033, Japan

[5]Lead Contact

Correspondence: tsengoku@yokohama-cu.ac.jp (T. S.)

Summary

Human herpesviruses (HHVs) are widespread pathogens causing severe diseases, especially in immunocompromised individuals, and are linked to neurodegenerative and autoimmune disorders. Current antiviral therapies primarily target the α-subfamily, with limited options for β- and γ-subfamilies. The helicase-primase complex (HPC) is essential for viral DNA replication and represents a key antiviral target, but its structure and inhibition mechanisms were previously unclear. Here, cryo-EM structures of the HHV1 (α-subfamily) HPC bound to single-stranded DNA and two clinical inhibitors, amenamevir and pritelivir, are reported. The HPC features flexible helicase and primase modules, with both inhibitors binding a shared allosteric pocket in the helicase module. Structural, biochemical, and molecular dynamics analyses indicate that these inhibitors lock the helicase in an open, inactive conformation. Combined molecular dynamics and fragment molecular orbital analyses explain the α-subfamily selectivity and distinct antiviral spectra of these drugs. These findings provide a structural framework to guide the development of novel inhibitors targeting β- and γ-subfamily herpesviruses.

36 **Significance**

37 Herpesviruses are ubiquitous human pathogens responsible for a wide spectrum of diseases,
38 including severe infections in immunocompromised individuals and associations with
39 neurodegenerative and autoimmune disorders. Despite the clinical importance of these
40 viruses, current antiviral therapies are largely limited to the α-subfamily, with few effective
41 options for β- and γ-subfamilies. The helicase-primase complex (HPC) is a critical enzyme
42 for viral DNA replication and a validated antiviral target, yet its structural basis and
43 inhibition mechanisms have remained elusive, hindering the rational development of next-
44 generation therapeutics. This study provides the first high-resolution cryo-EM structures of
45 the human herpesvirus 1 (HHV1) HPC bound to single-stranded DNA and two clinically
46 relevant inhibitors, amenamevir and pritelivir. These structures reveal the modular
47 organization of the HPC and identify a shared allosteric pocket where both inhibitors bind.
48 Structural, biochemical, and molecular dynamics analyses demonstrate that these inhibitors
49 lock the helicase in an open, catalytically inactive conformation, thereby blocking ATP
50 binding and halting DNA unwinding. Fragment molecular orbital (FMO) calculations
51 further elucidate the molecular determinants of inhibitor binding, explaining the α-
52 subfamily specificity and the distinct antiviral spectra of amenamevir and pritelivir. The
53 integrated approach combining cryo-EM, molecular dynamics, and quantum chemical
54 calculations not only clarifies the mechanism of action of current clinical inhibitors but also
55 establishes a robust framework for the rational design of novel antivirals. By providing
56 detailed insights into the structural and dynamic properties of the HPC and its inhibition,
57 this work paves the way for the development of new drugs with tailored specificity and

58 improved pharmacokinetic properties, potentially expanding therapeutic options to
59 currently untreatable herpesvirus infections. These findings have broad implications for
60 antiviral drug discovery and for understanding the molecular mechanisms underlying DNA
61 replication in herpesviruses.

62 **Introduction**

63 Human Herpesviruses (HHVs) are significant human pathogens[1]. To date, eight
64 herpesviruses (HHV1–8) have been identified and classified into three subfamilies: α, β,
65 and γ. All these herpesviruses can cause human diseases, including herpes simplex, herpes
66 zoster, encephalitis, and various tumors. They can also lead to severe conditions,
67 particularly in immunocompromised individuals. Moreover, recent studies have suggested
68 potential links between herpesvirus infections and chronic diseases such as Alzheimer's
69 disease[2], dementia[3], multiple sclerosis[4], and chronic fatigue syndrome[5]. Currently, multiple
70 anti-herpes drugs, such as nucleoside analogs and helicase-primase inhibitors (HPIs), are
71 available for the α-subfamily (HHV1/HSV1, HHV2/HSV2, and HHV3/VZV). In contrast,
72 therapeutic options for the β-subfamily (HHV4/Epstein-Barr virus and HHV8/Kaposi's
73 sarcoma-associated virus) and γ-subfamily (HHV5/cytomegalovirus, HHV6, and HHV7)
74 remain limited, underscoring the need to develop new antiviral drugs targeting these
75 subfamilies.

76 Herpesviruses employ a set of unique enzymes for the replication of their genomes, which
77 can be therapeutically targeted by specific inhibitors. One such target is the helicase-
78 primase complex (HPC)[6], composed of three subunits: the helicase subunit (UL5 in
79 HHV1), the primase subunit (UL52 in HHV1), and a non-catalytic accessory subunit (UL8
80 in HHV1). The HPC associates with the replication fork and unwinds the DNA duplex
81 through the action of the helicase subunit, generating ssDNA as the templates for DNA
82 synthesis by the viral DNA polymerase. While most replicative helicases in eukaryotes and

83 prokaryotes form hexameric ring structures surrounding the DNA[7], herpesvirus helicases
84 belong to superfamily Ib, which is thought to function as monomers[8]. A previous studies on
85 a related superfamily Ib helicase has shown that they alternate between “open” and
86 “closed” conformations in an ATP hydrolysis-dependent manner, translocating along
87 ssDNA in an inchworm-like motion to separate the base pairs they encounter[9]. The HPC
88 also synthesizes an RNA primer on the lagging strand through the action of the primase
89 subunit. This subunit contains sequence motifs conserved among archaeo-eukaryotic
90 primases[10], along with a putative zinc-binding domain (ZBD), which is commonly found in
91 other primases, including the human PrimPol protein. Notably, all three subunits of the
92 HPC are required for the optimal activities of both the helicase and primase, suggesting
93 complex regulatory interactions between them. As no experimental structure of the HPC
94 has been determined, it remains elusive how these subunits interact with each other, how
95 the two catalytic domains are spatially arranged, and how the two activities are coordinated
96 within this unique complex.

97 HPIs specifically inhibit the HPC of α-subfamily, thereby suppressing their replication. One
98 such molecule, amenamevir (AMNV)[11,12] has demonstrated efficacy against all three α-
99 herpesviruses, HHV1 and 2 (also known as herpes simplex viruses 1 and 2, respectively),
100 and HHV3 (varicella zoster virus). AMNV has been approved in Japan for the treatment of
101 herpes simplex and herpes zoster; however, its poor brain penetration[13] limits its clinical
102 utility for treating herpesvirus-induced encephalitis. Pritelivir (PTV)[14,15], another clinical
103 HPI in phase 3, is effective against HHV1 and HHV2, but shows only limited activity
104 against HHV3 and HHV5[14]. To date, no HPIs effective against β- and γ-subfamily

105 herpesviruses have been reported. The lack of structural analysis of the interaction between
106 α-herpesvirus HPC and HPI has hindered rational design of next-generation HPIs effective
107 against β- and γ-subfamily herpesviruses.

108

109 **Results**

110 **Overall structure**

111 To elucidate the overall architecture of the HPC and the inhibition mechanism by HPIs, we
112 set out to determine its cryo-EM structures. We reconstituted the HPC of HHV1 by co-
113 expressing the three subunits in insect cells and purified the complex by affinity
114 chromatography. We mixed the purified HPC with a 43-mer ssDNA, AMP-PNP (a
115 nonhydrolyzable analog of ATP) and either AMNV or PTV, and collected cryo-EM images.
116 During the EM volume reconstruction, we noticed that the HPC can be divided into two
117 modules, hereafter referred to as the helicase module (HM) , consisting of the entire UL5
118 (helicase) and two domains of UL52 (primase), and the primase module (PM), consisting of
119 the primase domain of UL52 and the entire UL8 (non-catalytic subunit). The relative
120 positions of the two modules are flexible. Thus, following the global density reconstruction,
121 focused refinement of the two modules was independently performed, yielding two locally
122 refined maps with improved resolution (about 2.9-3.3 Å), on which we built atomic models
123 (Figure S1-S5). We also performed a 3DFlex refinement[16] of the overall complex which
124 gave a better overall resolution (about 3.1-3.3 Å) and built the full atomic models into these
125 3DFlex maps with the help of the two atomic models built on locally refined maps

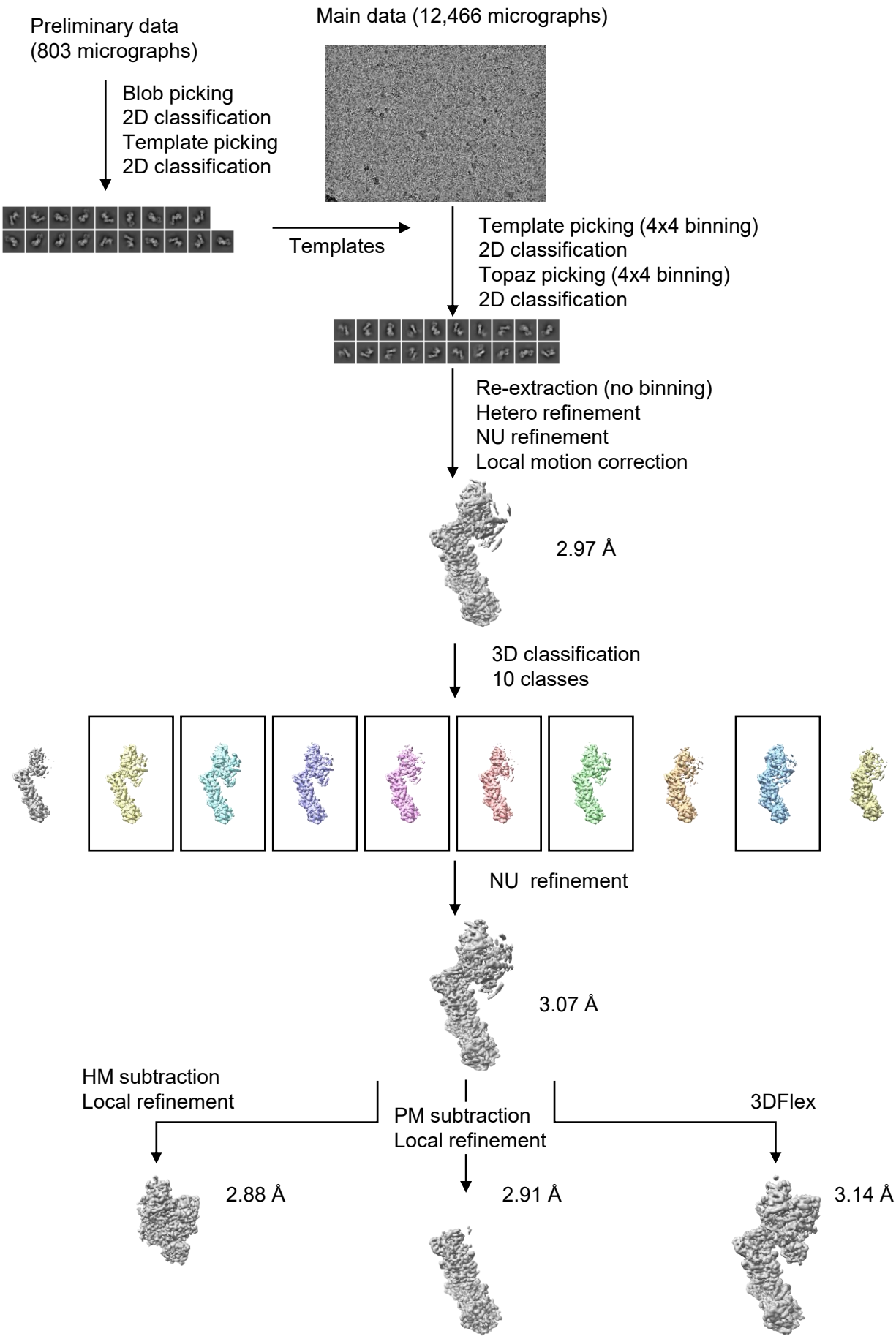

Figure S1: Cryo-EM data processing of the AMNV complex, related to Figure 1.

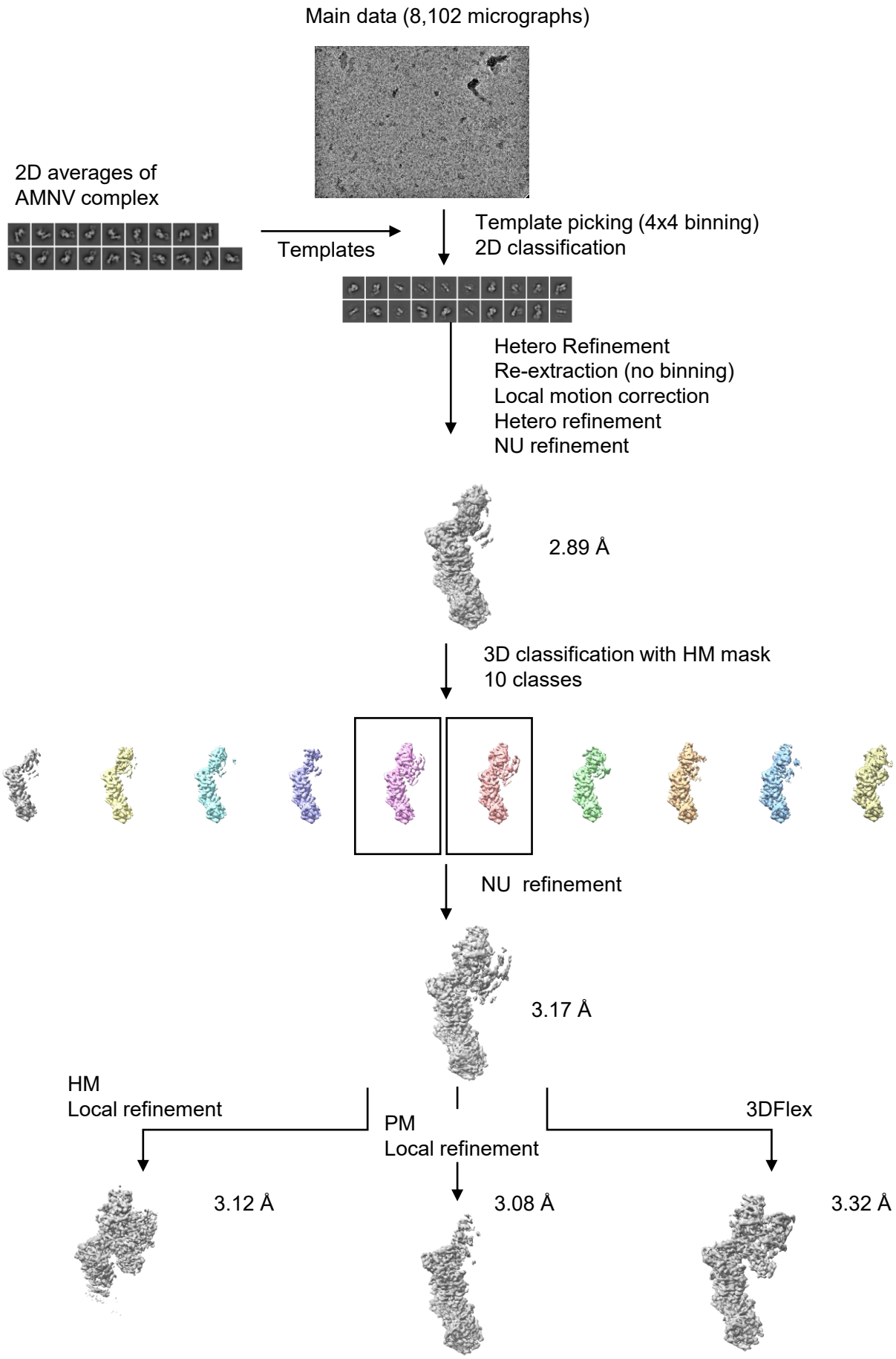

Figure S2: Cryo-EM data processing of the PTV complex , related to Figure 1.

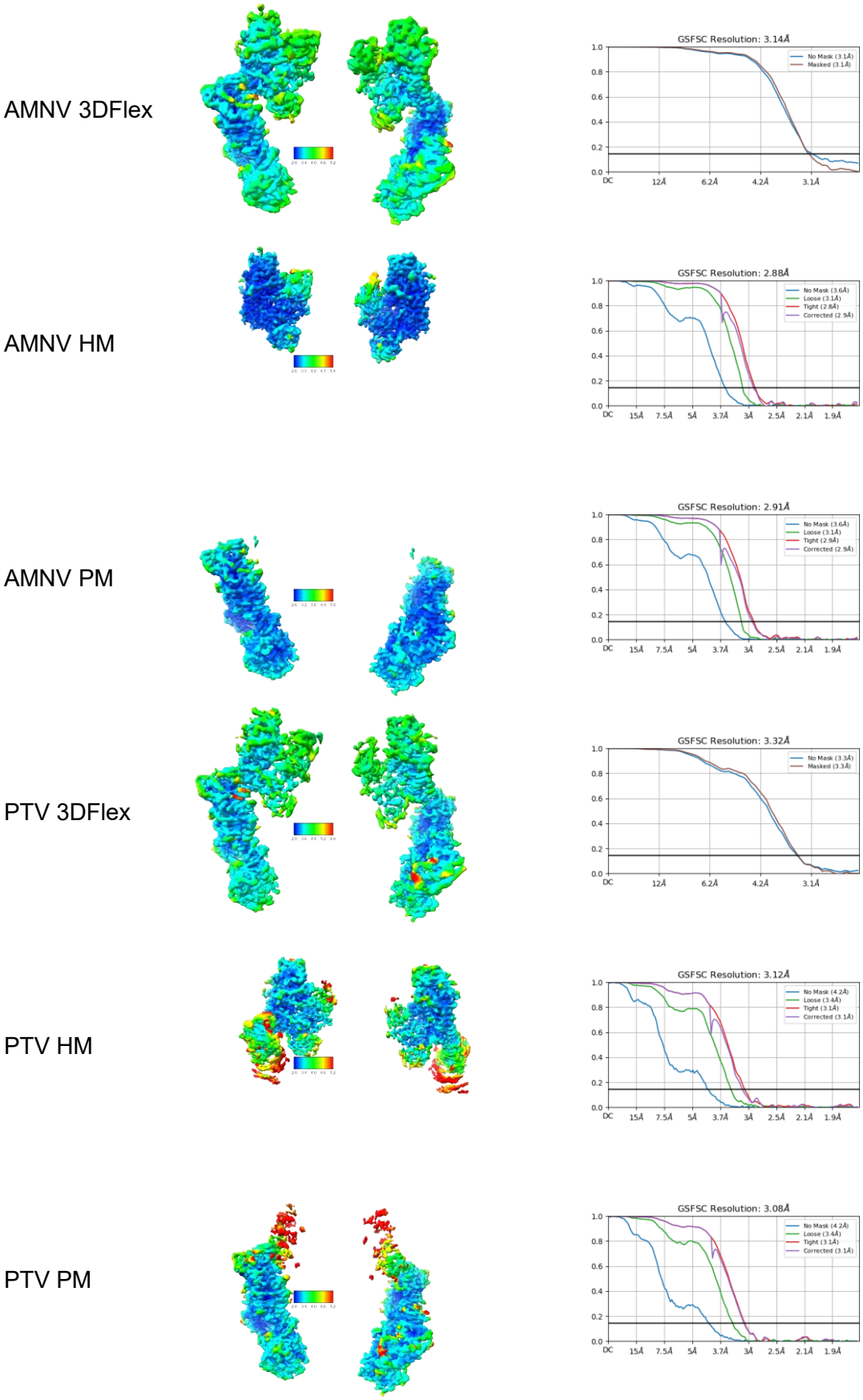

Figure S3: Cryo-EM maps and resolutions of the AMNV and PTV complexes , related to Figure 1.

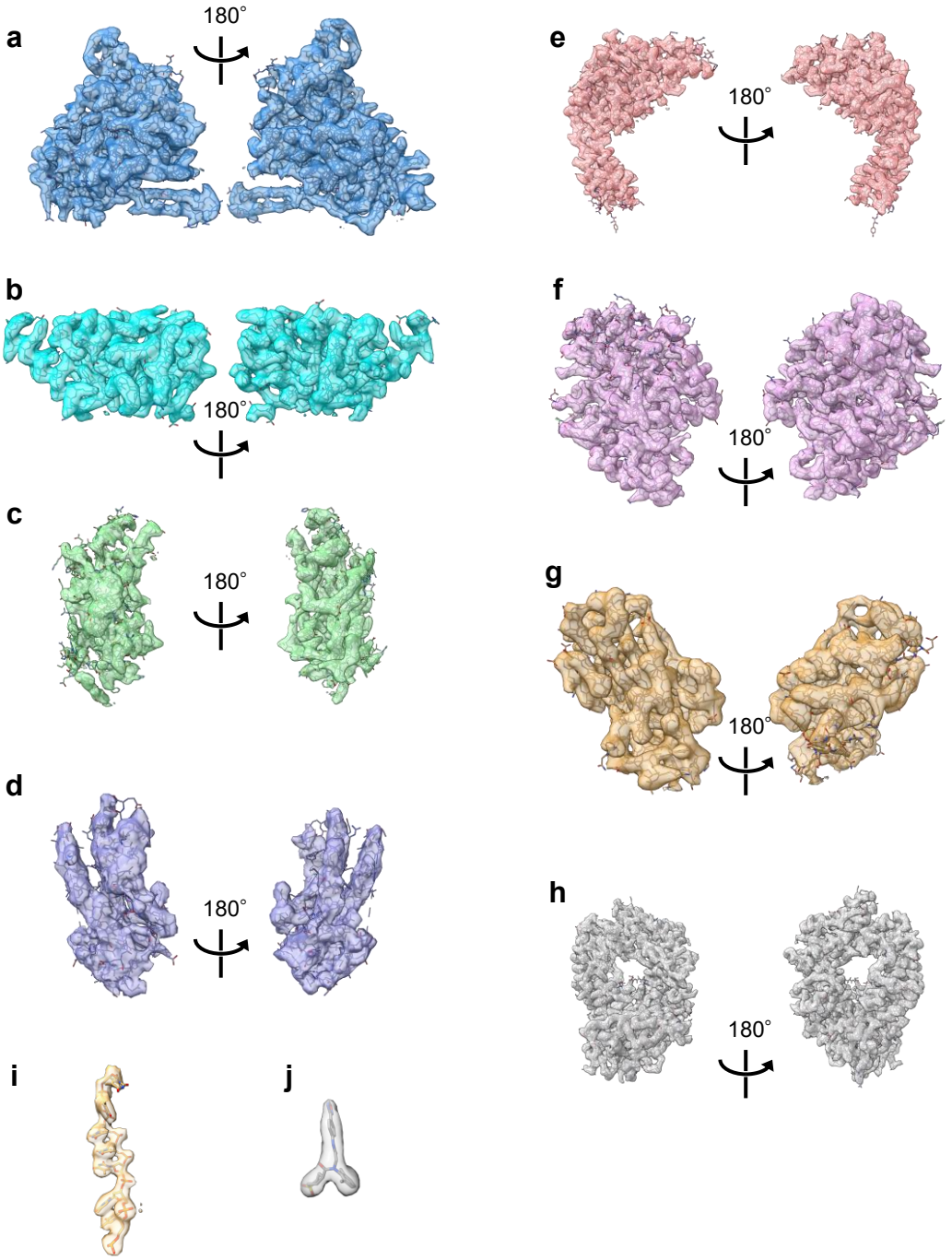

Figure S4: Locally refined maps of individual domains of the AMNV complex, , related to Figure 1. a, 1A. **b**, 2A. **c**, 2B. **d**, 2C. **e**, SD. **f**, PD. **g**, ZBD. **h**, UL8. **i**, ssDNA. **j**, ANMV.

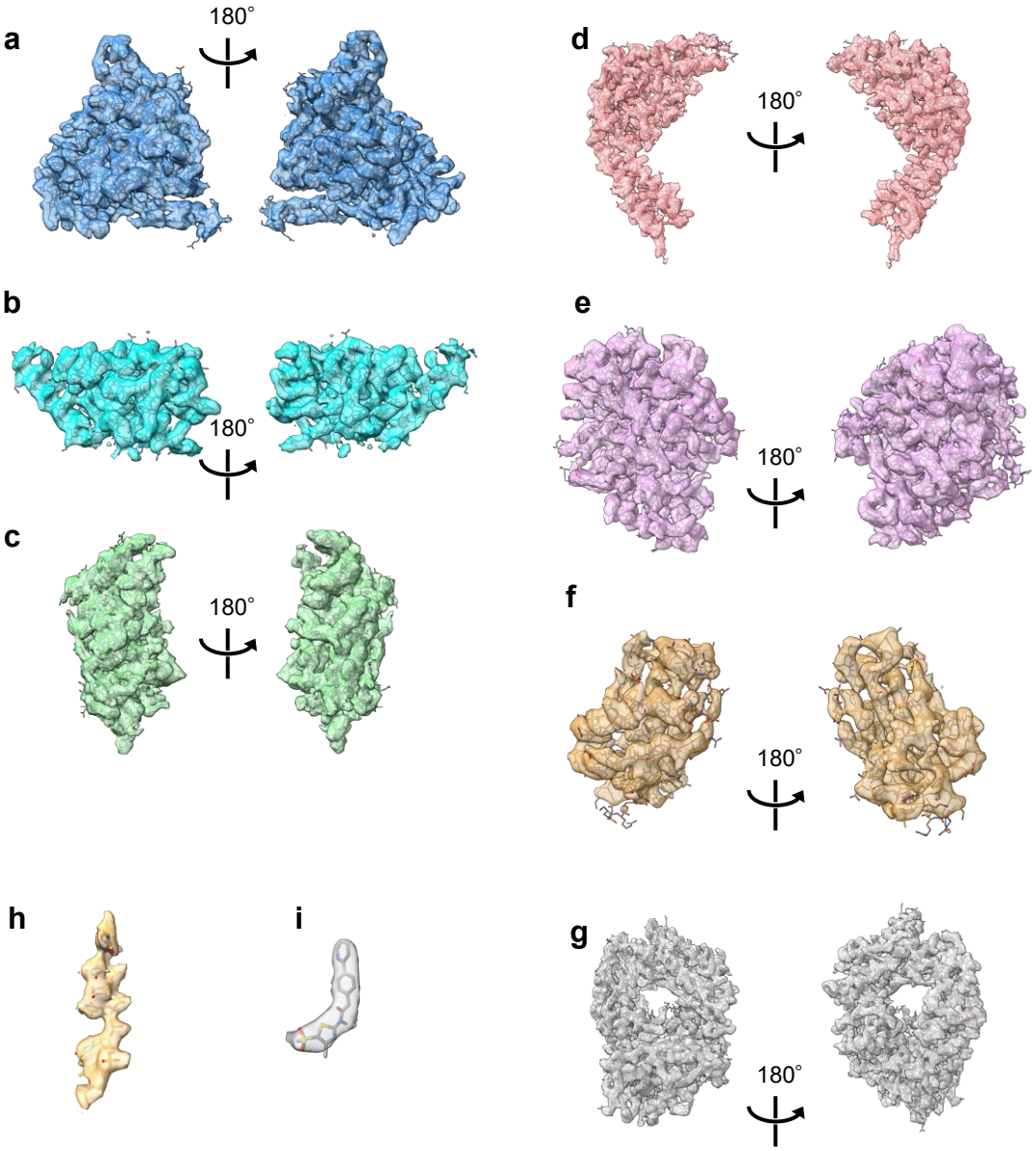

Figure S5: Locally refined maps of individual domains of the PTV complex, , related to Figure 1. No model was built for the domain 2C on the locally refined map of the helicase module of the PTV complex because of poor resolution. **a**, 1A. **b**, 2A. **c**, 2B. **d**, SD. **e**, PD. **f**, ZBD. **g**, UL8. **h**, ssDNA. **i**, PTV.

126 (Supplementary Movie 1). Unless otherwise stated, we use locally built models to describe
127 local interactions and the 3DFlex-derived models for discussion on global structures.

128 Figure 1 and Figure S6 show the overall structures of the AMNV- and PTV-bound
129 complexes, respectively. The HM consists of the entire UL5 protein and two domains of
130 UL52, namely the scaffold domain (SD, residues 1-408 and 891-910) and the ZBD
131 (residues 911-1043). The two domains of UL52 intimately interact with UL5 with large
132 interface areas. UL5 consists of the domains 1A (residues 34-344 and 864-892), 2A
133 (residues 345-417 and 805-863), 2B (residues 418-514 and 693-804), and 2C (residues
134 515-692), which are shared by superfamily Ib helicases. Structure similarity analysis using
135 the DALI server[17] revealed that the helicase subunit is most similar to Pif1 helicases (e.g.,
136 PDB ID: 7OTJ; Z score = 19.2)[18–21]. Of the 43-mer ssDNA used for structural
137 determination, only seven nucleotides were clearly visible, bound to domains 1A, 2A, and
138 2B of UL5, with the 5′ and 3′ ends bound to domains 2A and 1A, respectively, in agreement
139 with other superfamily I and II helicases[8]. We tentatively modeled them as oligo-dT.
140 Notably, no density of AMP-PNP was observed at the ATPase active site of UL5 (discussed
141 later). The PM consists of the primase domain of UL52 (PD, residues 409-890) and the
142 entire UL8 protein, which interact with each other. The intimate interaction between UL5-
143 UL52 and UL52-UL8 explains why a lack of one subunit seriously affects the helicase and
144 primase activities of the remaining subunits.

145 AMNV and PTV bind to a shared pocket located near, but not at, the ATP-binding site. The
146 pocket is formed by the SD of UL52 and the linker region connecting domains 1A and 2A

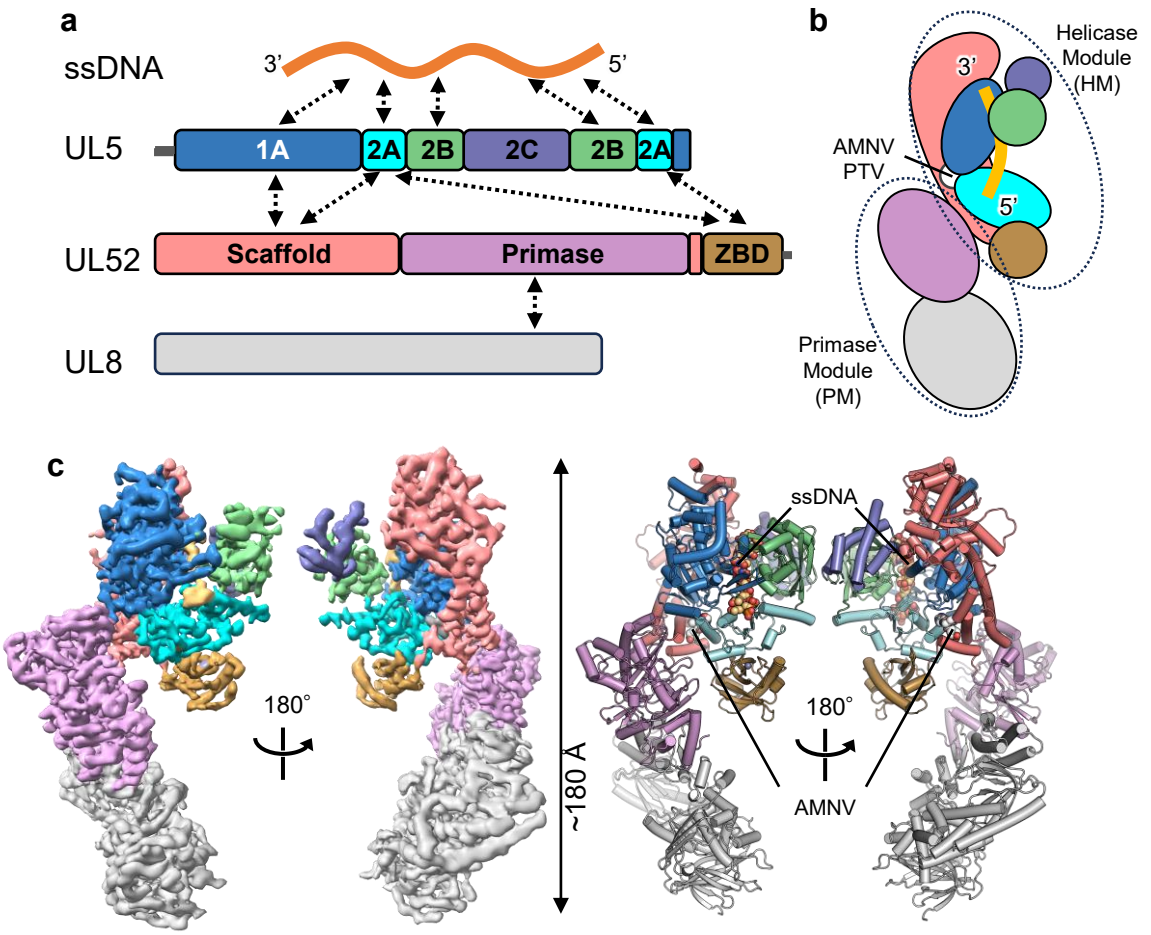

Figure 1: Overall structure of the AMNV-bound HPC from HHV1. a, Domain architectures of the three subunits and their interactions with each other and with ssDNA. The color scheme used in this panel is applied consistently throughout the paper to distinguish different domains. **b**, A cartoon illustration of the HPC. **c**, 3DFlex map (calculated using 3DFlex) and the ribbon model of the AMNV-bound HPC.

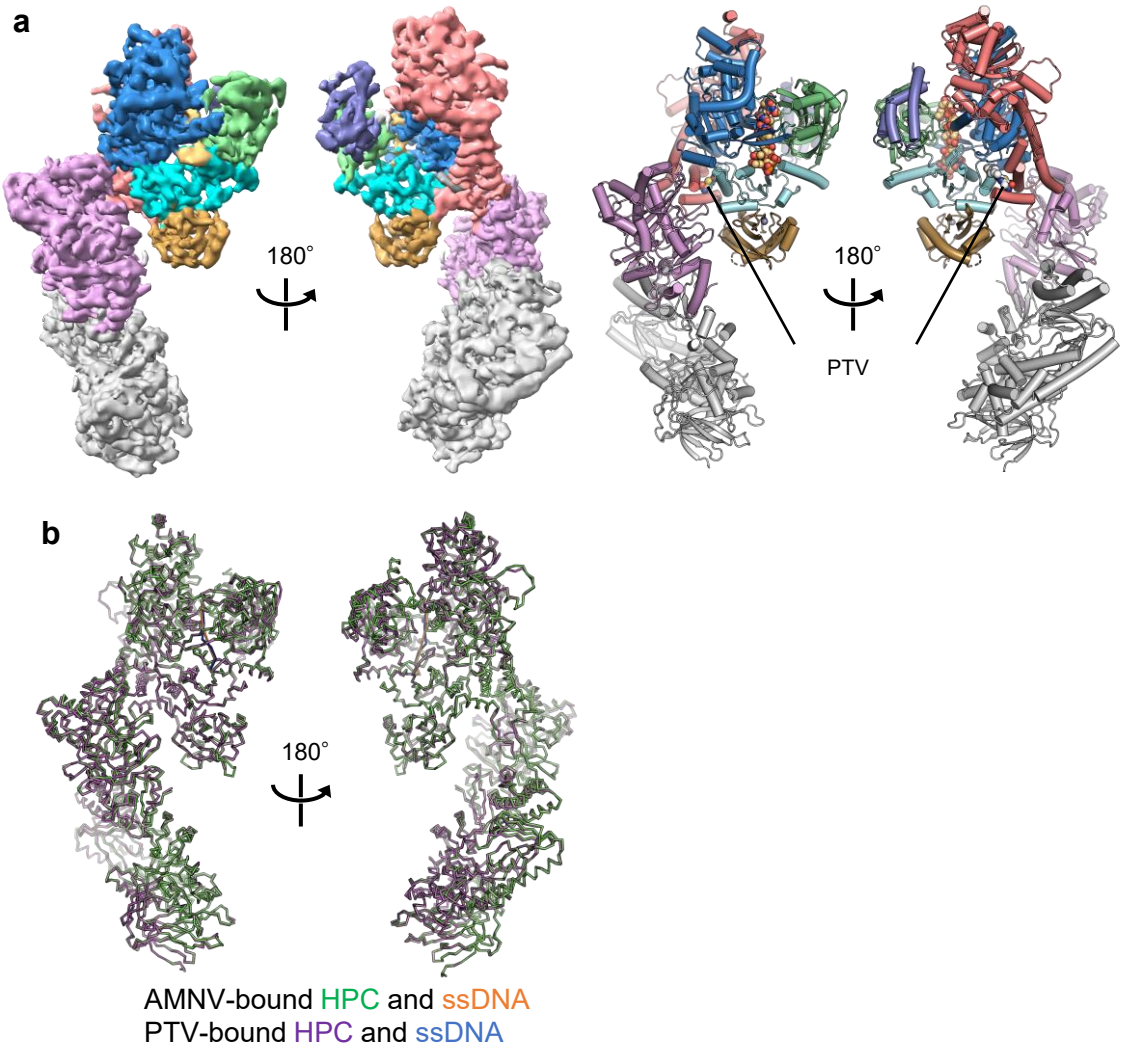

Figure S6: Structure of the PTV-bound HPC, , related to Figure 1. a, 3DFlex map (calculated using 3DFlex) and the ribbon model. **b**, Structural superposition of the AMNV- and PTV-bound complexes.

147 of UL5 (designated as motif IIIa in superfamily I, although sometimes referred to as motif
148 IV)[8]. In the structures of superfamily Ia and Ib helicases[9,20,22], a conserved arginine residue
149 of motif IIIa (corresponding to R345 of UL5) directly interacts with the γ-phosphate group
150 of the bound ATP analogs. This suggests that motif IIIa plays a role in coupling ATP
151 binding/hydrolysis to domain movement—a process potentially influenced by binding of
152 HPIs. The two inhibitor-bound structures are nearly identical (the RMSD value of 0.50 Å
153 for 1,098 Cα atoms of the HM; Figure S6), suggesting that the two inhibitors likely
154 function in essentially the same manner. Most of the known single-point resistance
155 mutations to AMNV or PTV map directly to this inhibitor-binding pocket, suggesting their
156 physiological binding (see "Binding and specificity of HPIs").

157 **PD and ZBD of UL52**

158 The DALI server search revealed that the PD is structurally similar to other archaeo-
159 eukaryotic primases, including human and bacterial PrimPol (e.g., PDB ID: 5L2X; Z-score
160 = 14.8) as well as viral helicase-primase fusion proteins (e.g., PDB ID: 8XJ6; Z-score =
161 12.7) whose helicase domains assemble into a hexameric ring. When a template DNA-
162 bound structure of PrimPol[23] is superposed, the superposed DNA is positioned with its 3'
163 end directed towards the HM, while the HM-bound ssDNA in the current HPC structure is
164 oriented with its 5' end toward the PM (Figure S7a-c). This configuration is consistent with
165 a model in which a single HPC molecule engages the continuous template strand via its
166 HM and PM simultaneously. However, to accommodate a single ssDNA spanning the two
167 modules in a smooth conformation, substantial reorientation between these two modules

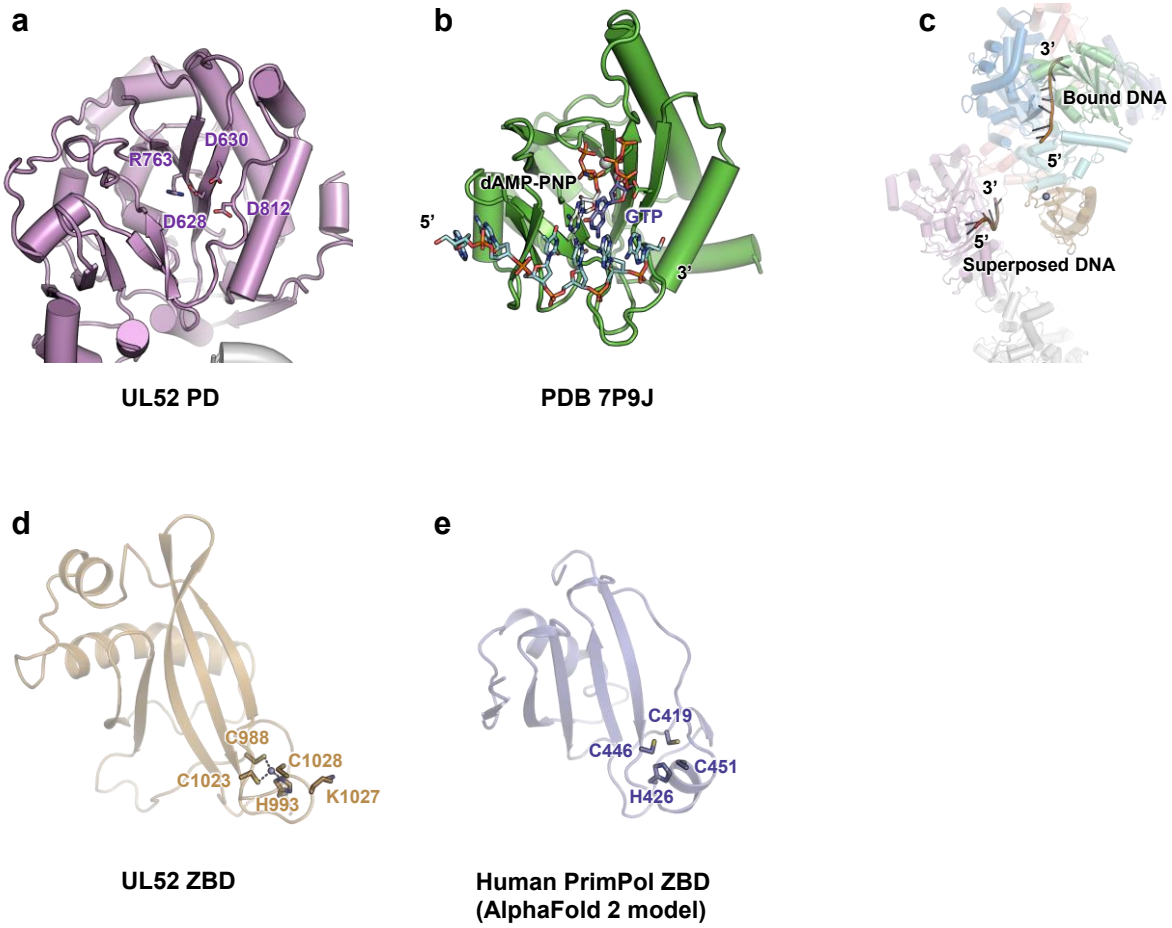

Figure S7: Structures of the PD and ZBD, , related to Figure 1. a, Structure of the PD. Key catalytic residues conserved among archaeo-eukaryotic primases are shown. **b**, Structure of the primer initiation complex of Prim-Pol domain of CRISPR-associated Prim-Pol (PDB 7P9J). The bound template DNA and two nucleotides (GTP and dAMP-PNP at the initiating and elongating sites, respectively) are also shown. **c**, Superposition of the structures of the AMNV-bound HPC and the template-bound Prime-Pol (only template DNA is shown). **d**, Structure of the ZBD of UL52 in the AMNV-bound HPC. Four zinc-coordinating residues as well as K1027, whose substitution abolishes the activities of HPC, are shown. **e**, A predicted structure of the ZBD (residues 366-468) of human PrimPol (UniProt Q96LW4), downloaded from AlphaFold Protein Structure Database. Possible zinc-coordinating residues are shown.

168 would be necessary. Given the apparent flexibility between the two modules and the lack of
169 a large interaction surface between them, it is possible such reorientation occurs during the
170 productive primer synthesis by the PD coupled with replication fork progression driven by
171 the HM. The HPC may engage the template DNA through an alternative mechanism (e.g.,
172 two HPC molecules binding to a single replication fork), as suggested earlier[24].

173 The ZBD coordinates a zinc ion via C988, H993, C1023, and C1028. The UL52 ZBD is
174 widely conserved among eukaryotic PrimPol proteins. Structural prediction using
175 AlphaFold2[25] revealed a strong similarity between the ZBD of UL52 and that of human
176 PrimPol (Figure S7d, e). The human PrimPol ZBD possesses ssDNA-binding activity and
177 is required for primase activity. It has been proposed to bind template ssDNA to regulate
178 the primase and polymerase activities of PrimPol[26]. The reorientation of the HM and PM
179 domains may bring the PD and ZBD closer together, enabling such a cooperative binding
180 mode.

181 **UL8-PD interactions**

182 As predicted by a previous bioinformatic analysis[27], UL8 adopts a fold that is structurally
183 related to B-family DNA polymerases. However, UL8 lacks both the catalytic residues
184 required for coordinating divalent ions and the basic surface necessary for template DNA
185 binding (Figure S8), consistent with its lack of detectable enzymatic activity. At the UL52–
186 UL8 interface, a network of salt bridges and hydrogen bonds is formed, involving the R640
187 side chain and L748 main chain of UL8, and the side chains of E511 and R437 of UL52
188 (Figure S8c). Notably, R640 is one of five residues that are completely conserved among

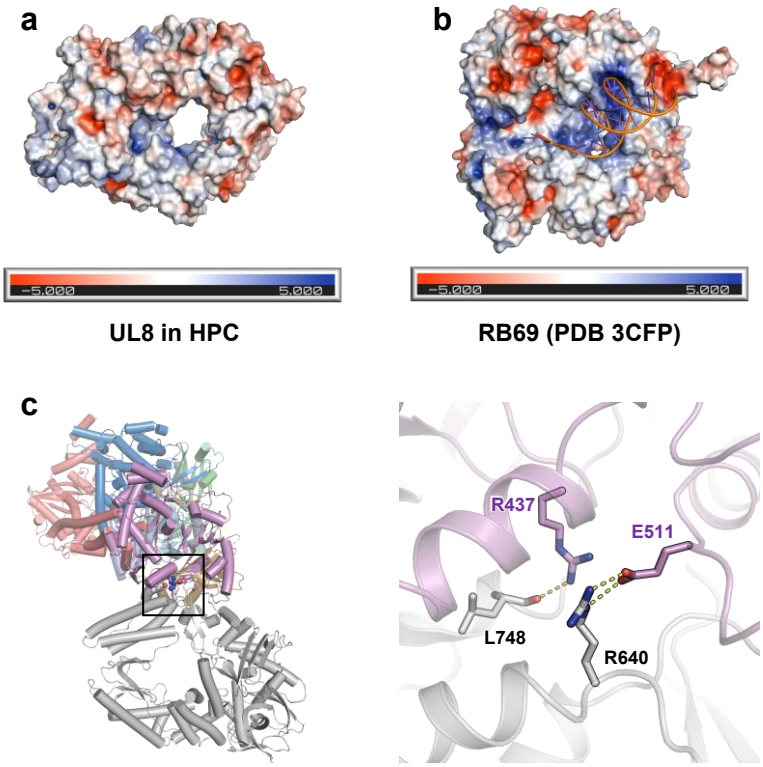

Figure S8: Structure of UL8 , related to Figure 1. a and **b**, Electrostatic surface potentials of UL8 (**a**) and RB69 (**b**), an α family DNA polymerase, bound with a DNA duplex. **c**, The UL52-UL8 interface. Left, the overall structure of HPC with the UL52-UL8 interface highlighted by a box. Right, A close-up view of the boxed region.

189 the eight human herpesviruses and was previously predicted to be involved in UL52
190 binding based on a mutagenesis study[28].

191 **Helicase module and ssDNA binding**

192 The bound ssDNA interacts with the domains 1A, 2A, and 2B of UL5. Domains 1A and 2A
193 engage the DNA backbone mainly through hydrophilic interactions with the phosphate
194 groups, while domain 2B mostly forms van der Waals contacts with it (Figure 2a-e).
195 Nucleotides dT3-dT5 are wrapped around by the three domains and completely buried
196 within a channel that is too small to accommodate the double-stranded DNA (Figure 2a),
197 suggesting that like other superfamily I helicases, UL5 unwinds the DNA duplex via a
198 steric exclusion mechanism coupled with the translocation along the tracking strand.
199 Domain 2A binds the phosphate groups of dT2-dT4 via the conserved helicase motifs IV
200 and V, whereas domain 1A binds those of dT5-dT7 via motifs Ia and Ic. This binding mode
201 resembles those observed in other superfamily Ib helicases such as RecD2 and Pif1[9,18–20].
202 Substitution of T809 (motif V) with isoleucine was shown to impair viral DNA replication
203 and reduce both ATPase and helicase activities of the UL5-UL52 subcomplex[29,30].

204 The bound DNA is slightly curved, and base-stacking interactions are interrupted between
205 dT2 and dT3 and between dT5 and dT6 (Figure 2b-e). Two structural elements, the motif Ic
206 helix (residues 153-156) in domain 1A and a β-hairpin (residues 298-313, unique to UL5)
207 of domain 2A, are inserted between the neighboring bases at these positions, respectively,
208 likely stabilizing the curved conformation. Interrupted base stacking is commonly seen in
209 superfamily I and II helicases and may have an important role in DNA unwinding[8].

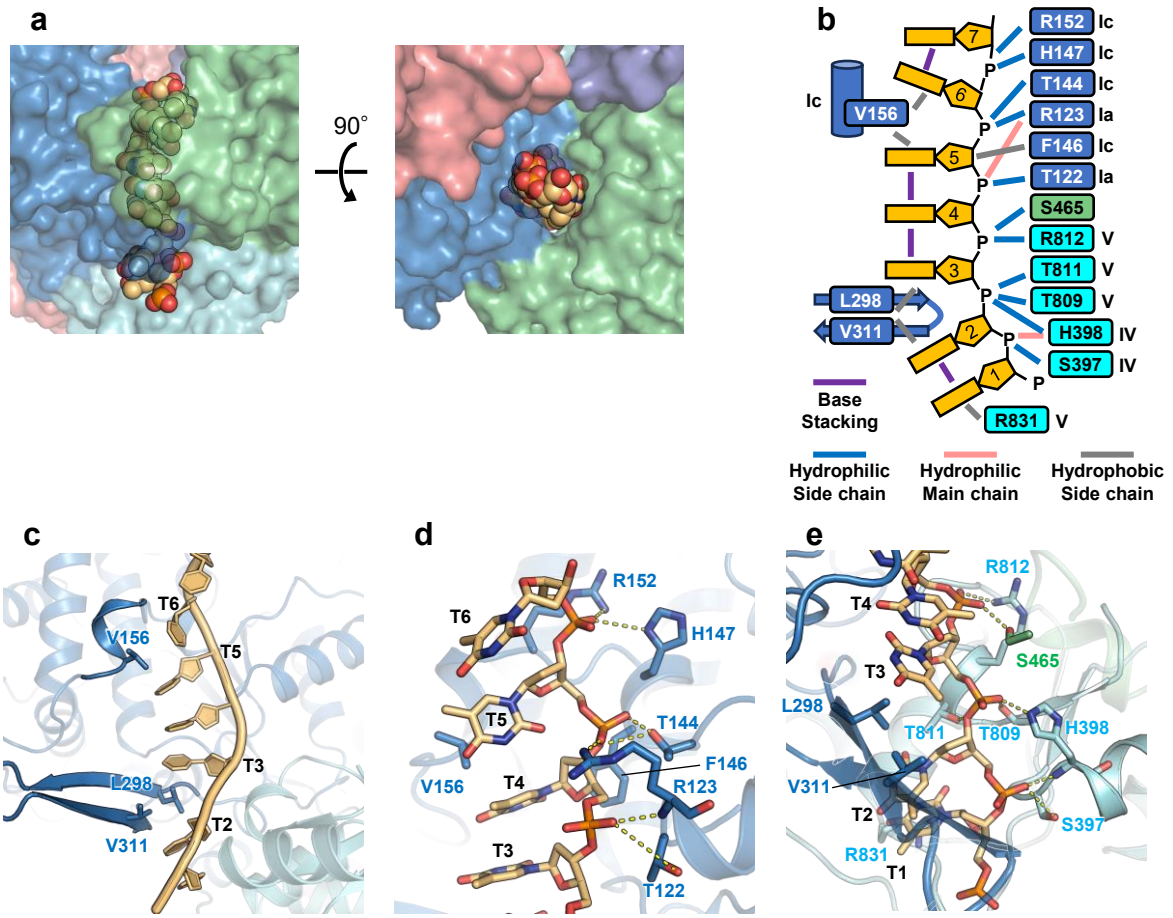

Figure 2: UL5-DNA interaction. a, The bound ssDNA is wrapped by domains 1A, 2A, and 2B (two views). UL5 and ssDNA are shown as a transparent surface model and a sphere model, respectively. **b**, Schematic representation of ssDNA-UL5 interaction. **c**, Two structural motifs interfering with base-stacking interactions. **d** and **e**, Interactions between ssDNA and domain 1A (**d**) or domain 2A (**e**).

210 The platform domain of UL52 is L-shaped and mostly α-helical. The DALI[17] search found
211 no hit with comparable side and Z-score > 6.5, indicating that the PD is likely a novel fold.
212 The PD interacts with the UL5, with a large interaction area, and with inhibitors (Figure
213 1c).

214 **Domains 1A and 2A adopt an open form in the HPI-bound HPC**

215 During their catalytic cycle, superfamily I helicases undergo conformational changes
216 between an ATP-bound closed form and an ATP-free open form [8,22]. The ATPase site
217 comprises motifs I (also known as P-loop or Walker A motif), Ia, II (also known as DEXX
218 motif or Walker B motif), III, IIIa, V, and VI, which are distributed along the cleft between
219 domains 1A and 2A. ATP binding induces closure of this cleft, resulting in the formation of
220 a functional ATPase site contributed by both domains. The essential roles of these residues,
221 including the motif I lysine (K103 of UL5), the motif II aspartate and glutamate (D249 and
222 D250 of UL5), and the motif VI arginine (R841 of UL5) have been demonstrated by
223 mutational studies on UL5[29,30] or related superfamily I helicases[18,31]. Structural studies of
224 superfamily Ia and Ib helicases[9,22] have shown that motif I and motif II are involved in
225 binding the triphosphate moiety and the catalytic magnesium ion, respectively, whereas the
226 arginine in motif VI functions as the so-called "arginine finger"[8], contacting the
227 triphosphate moiety in the ATP-bound closed form.

228 To gain insights into the mode of action of HPIs, we compared the current AMNV-bound
229 HPC structure with that of the structurally most related helicase, Pif1[20]. In both the AMNV-
230 bound HPC and the open form of Pif1, motifs Ia (domain 1A) and IV (domain 1B) contact

231 the bound ssDNA phosphates that are separated by three nucleotides (Figure 3a, b). In
232 contrast, in the closed form of Pif1, the distance between these motifs corresponds to two
233 nucleotides (Figure 3c). This structural comparison clearly shows that the current HPC
234 structures represent an open form. Since the structure of ATP-free HPC in the absence of
235 HPIs has not yet been determined, it remains unclear how closely the current HPI-bound
236 structures resemble the functional ATP-free form in the catalytic cycle.

237 We also compared the conformations of the ATPase site among the three structures (Figure
238 3d-f). In the closed form of Pif1, the bound ATP analog (ADP-AlF_4^-) is surrounded by
239 residues from both domains 1A and 2A, including residues from motifs I (K97, contacting
240 phosphates), II (D171 and E172, chelating Mg^{2+}), and VI (R462, contacting the γ-phosphate
241 analog). In contrast, in the open form of Pif1, the two domains are separated, and the side
242 chain of R462 is too distant to contact the phosphate groups of the ADP bound to domain
243 1A. Similarly, in the AMNV-bound HPC structures, the corresponding catalytic residues
244 from motifs I (K103), II (D249 and E250), and VI (R841) are also too far apart to
245 coordinate ATP binding. Notably, although 1 mM AMP-PNP was added to the cryo-EM
246 samples, no density was observed at the ATPase site, suggesting that the current open form
247 of HPC has reduced affinity for ATP.

248 **HPIs allosterically and competitively inhibit ATP binding**

249 The open conformation observed in the HPI-bound HPC structures, along with the absence
250 of AMP-PNP density at the ATPase site, suggests that HPI binding alters the conformation
251 of the HPC, thereby allosterically reducing its affinity for ATP. To test this hypothesis, we

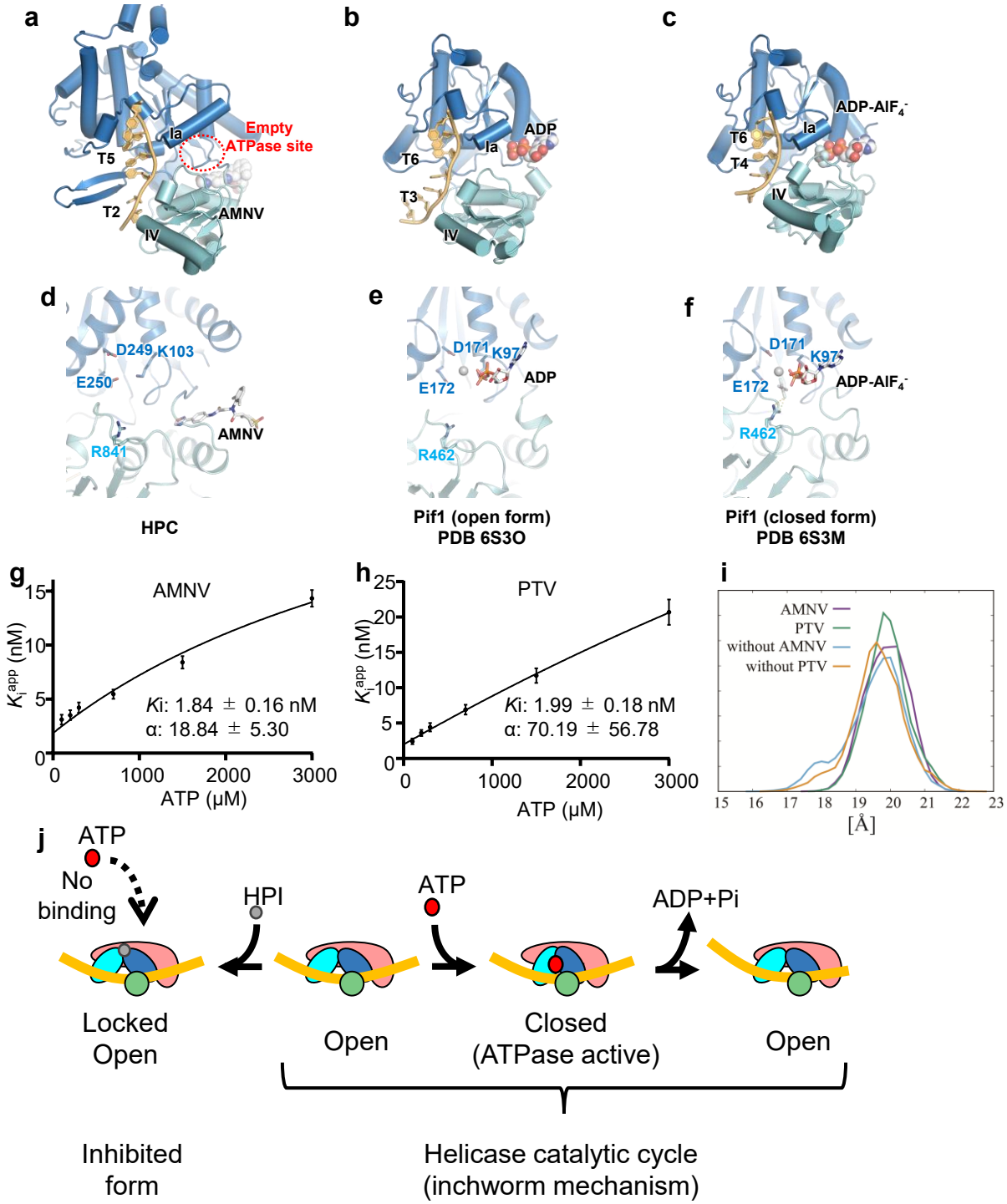

Figure 3: HPIs may lock UL5 in an open conformation. a-c, Structures of domains 1A and 2A in the ssDNA-bound states of the AMNV-bound HPC (**a**), ADP-bound Pif1 (**b**), and ATP analog-bound Pif1 (**c**). DNA nucleotides contacted by conserved residues in motifs Ia and IV (T122 and S397 of UL5 and their equivalents) are labeled. **d-f**, Close-up views of the ATPase site in the AMNV-bound HPC (**d**), ADP-bound Pif1 (**e**), and ATP analog-bound Pif1 (**f**). **g**, **h**, Relationship between ATP concentration and apparent inhibition constant (K_i^{app}), along with their standard error of the mean (SEM), in ATPase inhibition assays of AMNV (**g**) and PTV (**h**). The corresponding *Ki* and α values with SEM are also shown. **i**, Distribution of the distance between the centers of mass of K103, D249, and E250 in domain 1A and R841 in domain 2A during MD simulations. **j**, Proposed model for the inhibition mechanism of HPIs.

252 performed ATPase inhibition assays (Figure S9) using varying concentrations of ATP and
253 HPIs, and measured the effect of ATP concentration on the apparent inhibition constant
254 (K_i^{app}). As shown in Figure 3g and h, increasing ATP concentrations led to a corresponding
255 increase in K_i^{app}, suggesting that ATP and HPI binding are reciprocally inhibiting with each
256 other with respect to HPC affinity. We analyzed the inhibition data assuming a mixed
257 inhibition model, in which HPIs can bind both to the free HPC and to the HPC–ATP
258 complex[32]. From this analysis, we calculated the α factor, which represents how differently
259 inhibitors bind to the free HPC versus the HPC–ATP complex. Curve fitting yielded large α
260 factor values for both inhibitors (about 19 for AMNV and 70 for PTV), indicating that both
261 inhibitors bind to the free enzyme much more strongly, acting in a nearly ATP-competitive
262 manner, despite binding at the allosteric site.

263 **HPIs may lock the HPC in the open form**

264 Our structural and biochemical analyses suggest that HPIs affect the conformational
265 dynamics of the HPC by locking it in the open conformation observed in our cryo-EM
266 structures. To further substantiate our findings, we performed molecular dynamics (MD)
267 simulations on the following four systems (Figure S10a). The first two systems consist of
268 the UL5-UL52 subcomplex bound to ssDNA, with either AMNV or PTV (based on the
269 AMNV- or PTV-bound HPC structures, respectively). The remaining two systems are
270 identical to the first two, but lack the inhibitors, serving as controls.

271 For each system, we conducted eight replica MD simulations, each lasting 3 μs, and
272 analyzed the distance between key catalytic residues in domains 1A and 2A: K103, D249,

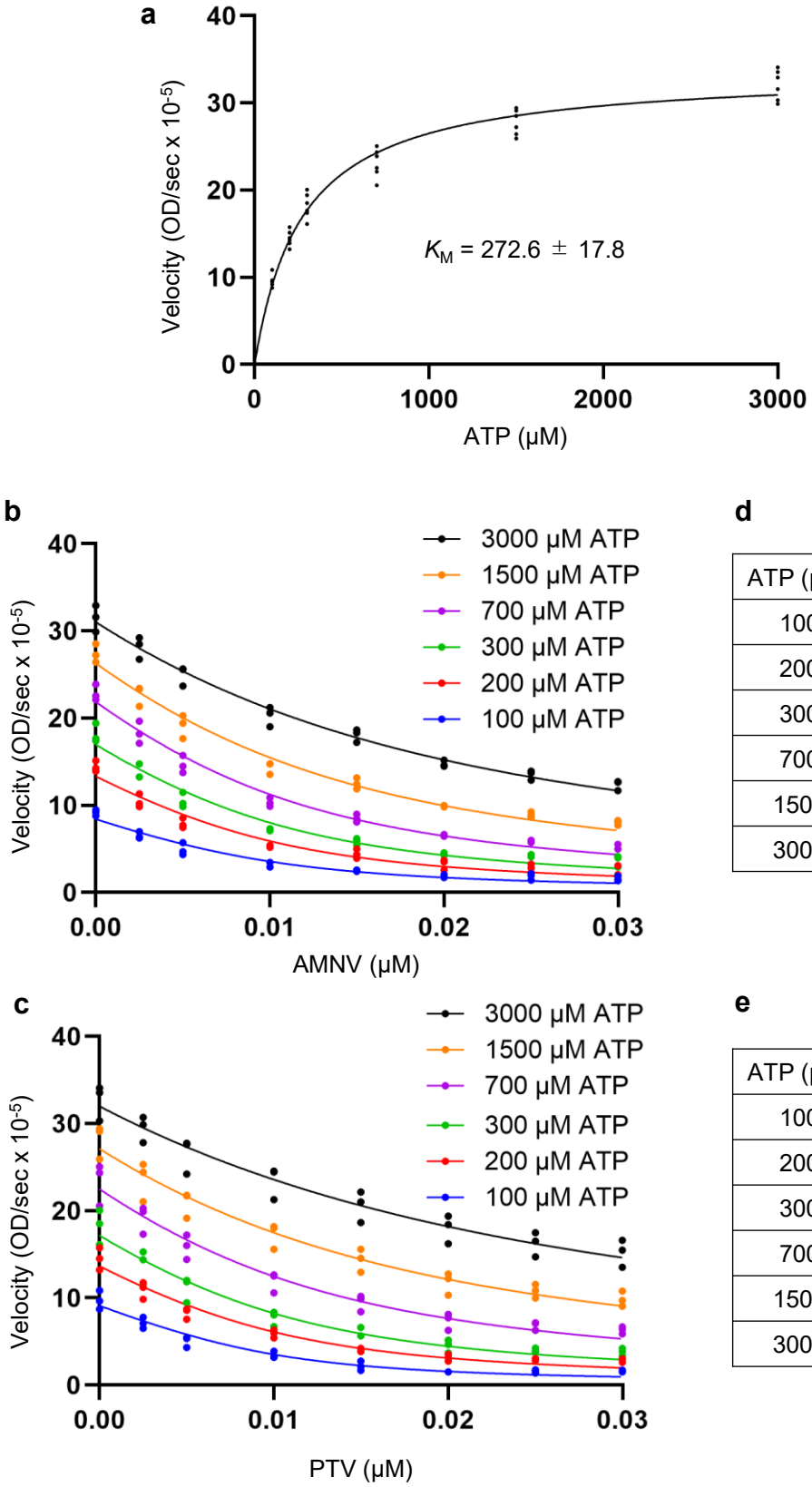

d

ATP (μM)	K_i^{app} (nM)
100	3.10 ± 0.46
200	3.52 ± 0.45
300	4.22 ± 0.48
700	5.47 ± 0.43
1500	8.41 ± 0.58
3000	14.34 ± 0.78

e

ATP (μM)	K_i^{app} (nM)
100	2.42 ± 0.40
200	3.61 ± 0.43
300	4.42 ± 0.60
700	6.90 ± 0.70
1500	11.72 ± 1.05
3000	20.67 ± 1.79

Figure S9: ATPase assays, related to Figure 3. ***a***, Michaelis-Menten plot used to determine the K_M value for ATP from six independent experiments. Standard error of the mean (SEM) is also shown. ***b*** and ***c***, Relationship between reaction velocity and the concentrations of AMNV (***b***) or PTV (***c***) at varying ATP concentrations. ***d*** and ***e***, K_i^{app} values of AMNV (***d***) and PTV € determined under different ATP concentrations. SEM is also shown.

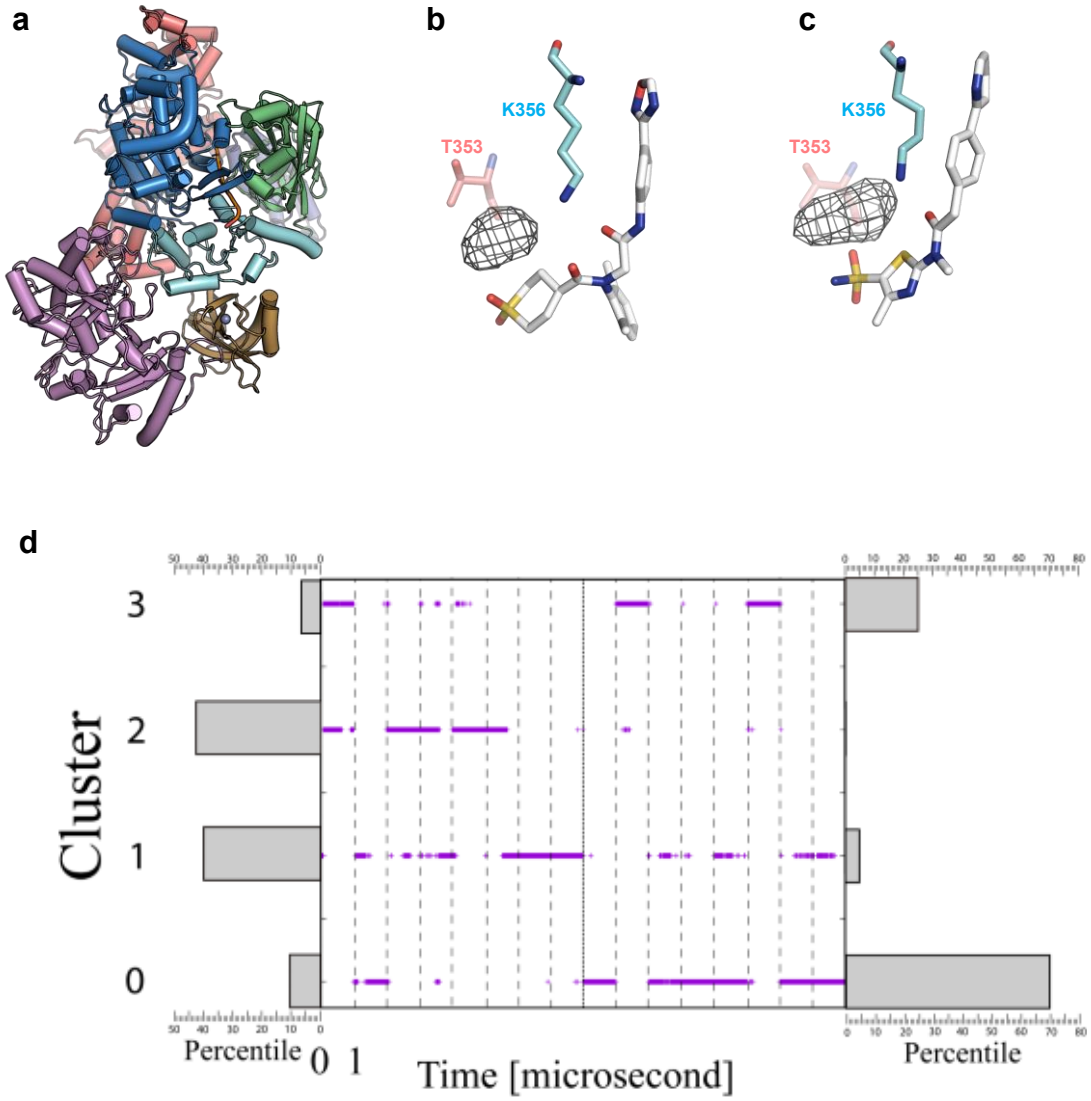

Figure S10: MD analysis , related to Figure 3. a, The modeled structure of the UL5-UL52 subcomplex for MD simulations. b and c, The water density (shown as white mesh, contour level 0.3) within 4.5 Å from the oxygen atoms of the sulfonyl oxygen of AMNV (b) or the sulfonamide NH2 group of PTV (c) are shown. d. The existence percentiles and time distributions of the four clusters for the AMNV and PTV complexes during the MD trajectories are shown on the left and right, respectively. Existence percentiles are represented by bars, while temporal distributions are plotted over time. Vertical dashed lines indicate the one-microsecond MD simulation boundary for each replica (8 replicas per system).

273 and E250 from motifs I and II in domain 1A, and R841 from motif VI in domain 1B
274 (Figure 3d). As shown in Figure 3i, the HPI-bound systems exhibited a unimodal
275 distribution of inter-residue distances, peaking around 20 Å. In contrast, the HPI-free
276 systems showed a bimodal distribution with peaks centered at approximately 18 Å and 19.5
277 Å. These results suggest that, in the absence of HPIs, domains 1A and 2A undergo
278 spontaneous conformational fluctuations that may potentially facilitate productive ATP
279 binding and hydrolysis. In contrast, HPI binding appears to restrict this flexibility,
280 stabilizing the HPC in an open, catalytically inactive conformation.

281 Based on these findings, we propose the following inhibition model (Figure 3j). In the
282 catalytic cycle of the inchworm model, the helicase alternates between open and closed
283 conformations, driven by ATP binding and hydrolysis. However, upon HPI binding, the
284 HPC is locked in the open conformation, thereby preventing ATP binding and stalling the
285 catalytic cycle. Consequently, the helicase remains inactive and unable to unwind DNA.

286 **Binding and specificity of HPIs**

287 Figure 4a-c shows the interactions between AMNV and PTV with the HPC, respectively. In
288 both complexes, two connected aromatic rings of each HPI are surrounded by residues
289 N98, N343, G352, M355, and K356 of UL5, as well as Y356 of UL52. AMNV and PTV
290 contain two and one carbonyl group(s), respectively, in their central regions, which are
291 within hydrogen-bonding distance of the UL5 K356 side chain. A sulfonyl group, which is
292 shared by both HPIs, forms a hydrogen bond with the side chain of UL52 N902. The
293 dimethylphenyl group, unique to AMNV, engages in hydrophobic interactions with the side

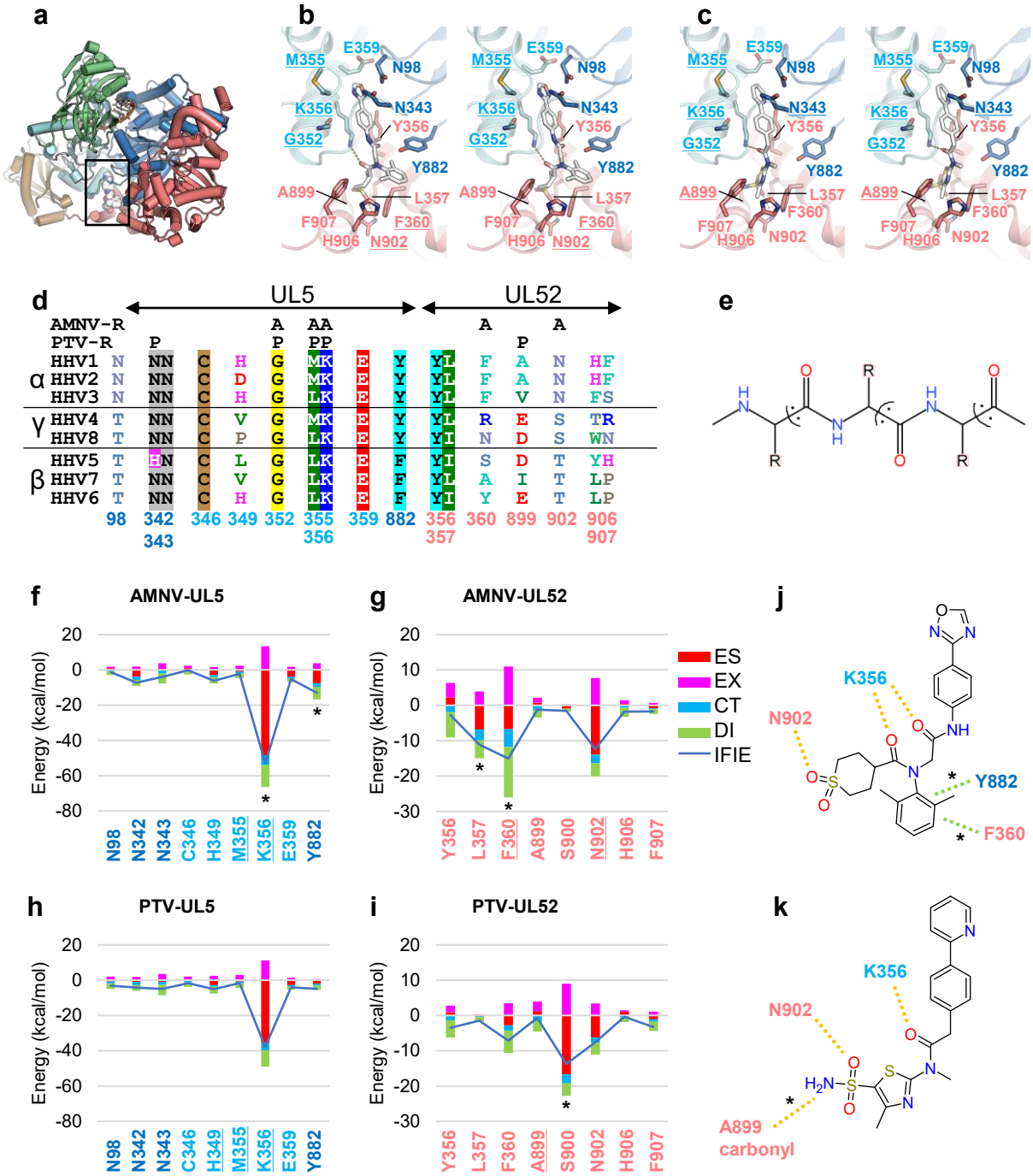

Figure 4: Binding and specificity of HPIs. a, Overall structure of the HPC, with the HPI binding site highlighted by a box. **b, c**, Stereo views of the binding site for AMNV (**b**) and PTV (**c**). Residues associated with resistance mutations are underlined. **d**, Sequence alignment of residues involved in HPI binding. “A” and “P” denote mutations that confer resistance to AMNV and PTV, respectively. **e**, Fragmentation scheme used for FMO calculations. **f–i**, PIEDA results showing interactions between AMNV and UL5 (**f**), AMNV and UL52 (**g**), PTV and UL5 (**h**), and PTV and UL52 (**i**). ES, EX, CT, and DI refer to the electrostatic, exchange-repulsion, charge transfer with higher-order mixing, and dispersion terms, respectively. Asterisks indicate residues contributing more than 5 kcal/mol to binding in one complex compared to the other. **j, k**, Schematic representations of the interactions between the HPC and AMNV (**j**) or PTV (**k**).

294 chains of UL5 Y882 and UL52 F360. Notably, most of the known single-point resistance
295 mutations of AMNV (G352C, M355T, and K356N in UL5, as well as F360V/C and N902T
296 in UL52)[33] and PTV (N342K, G352V, M355T, and K356Q in UL5 as well as A899T in
297 UL52)[14,34,35] are located at or near the binding site. N342K, G352C/V, and M355T in UL5
298 are expected to cause steric clashes at the HPI binding site, which may hinder HPI binding.
299 K356N/Q in UL5, as well as F360V/C and N902T in UL52, are predicted to disrupt critical
300 HPC–HPI interactions. These structural alterations likely account for their resistance
301 mechanisms. Although the HPI-contacting residues in UL5 are well conserved among all
302 human herpesviruses, those in UL52, such as F360, A899, N902, H906, and F907, are less
303 conserved (Figure 4d). This observation explains why the current HPIs are ineffective
304 against β- and γ-herpesviruses and provides a structural basis for the rational design of
305 novel HPIs targeting these subfamilies.

306 We next analyzed the MD trajectories to assess the potential contribution of water
307 molecules to the HPI binding. As shown in Figure S10b and c, a region of high water
308 density was observed in both complexes, where two water molecules bridge the side chain
309 of UL5 K356 and the sulfonyl group of the HPIs. Notably, these bridging water molecules
310 connect UL5 K356 and the sulfonyl group for 39.1% and 45.0% of the simulation time in
311 the AMNV and PTV complexes, respectively, suggesting the formation of a stable
312 hydrogen-bonding network. This water-mediated interaction may explain why the sulfonyl
313 group is essential for the tight binding of these inhibitors.

314 To quantitatively evaluate the differences between the AMNV and PTV-bound structures
315 and to gain mechanistic insights into their distinct anti-herpesvirus spectra, we performed
316 fragment molecular orbital (FMO) calculation analysis[36–39] on the representative structures
317 of MD trajectories. The FMO method divides biological macromolecules into residue-
318 based fragments (Figure 4e), thereby accelerating quantum chemical calculations and
319 enabling the extraction of inter-fragment interaction energy (IFIE) and its decomposition
320 data. To account for structural fluctuations in the HPI-HPC interactions, we clustered the
321 MD trajectories into four groups based on the coordinates of the HPI binding site (Figure
322 S10d), performed FMO calculations on the representative structures, and calculated the
323 weighted average energies, taking into account the existence probabilities of each cluster.

324 Figure 4f-i summarizes the FMO analysis results, showing the frequency-weighted average
325 values of IFIE and pair interaction energy decomposition analysis (PIEDA)[40] between
326 either AMNV or PTV and the UL5 and UL52 subunits. In agreement with our manual
327 inspection, residues involved in recognizing the common structural features of the two
328 HPIs are consistently identified in both complexes. These include residues surrounding the
329 two connected aromatic rings (UL5 N98, N343, and M355), UL5 K356 forming hydrogen
330 bonds with the HPIs' carbonyl oxygen, and UL52 N902 forming a hydrogen bond with the
331 sulfonyl oxygen.

332 In addition, comparison of the IFIE and PIEDA data (Figure 4f-i) reveals distinct binding
333 features of AMNV and PTV (summarized in Figure 4j, k). The stronger attractive
334 interaction energies for UL5 Y882 and UL52 F360 in the AMNV complex (by

335 approximately 8.1 and 7.9 kcal/mol, respectively), consisting of considerable dispersion
336 interaction energy (Figure 4f-i), indicate that the recognition of AMNV's unique
337 dimethylphenyl group by these residues via π-π and CH/π interactions, respectively (Figure
338 4b), substantially contributes to the binding affinity. Notably, these residues are conserved
339 across the α-subfamily, consistent with the AMNV's broad efficacy against all α-subfamily
340 members (Figure 4d). In contrast, UL52 S900 exhibits a stronger IFIE value in the PTV
341 complex, mainly due to electrostatic and charge transfer interactions, suggesting the
342 presence of the hydrogen bond[39]. In the FMO method, proteins are fragmented between the
343 α-carbon and carbonyl carbon, assigning the carbonyl group to the next residue (+1)
344 (Figure 4e). Structural analysis of the PTV complex revealed a hydrogen bond between the
345 A899 carbonyl group (assigned as S900 in the FMO scheme) and the PTV-specific NH_2
346 group of the sulfonamide moiety (Figure S11a). Structural modeling suggests that the
347 substitution of A899 with threonine (which confers PTV resistance) or with valine (the
348 corresponding residue in HHV3, Figure 4d) introduces steric hinderance that disrupts this
349 interaction (Figure S11b, c). Moreover, the A899T substitution does not confer resistance to
350 BILS 22 BS, another HPI that retains a sulfonyl group but lacks the NH_2 group[35].
351 Collectively, these findings indicate that the unique hydrogen bond between the NH_2 group
352 of PTV and the A899 carbonyl oxygen is critical for its inhibitory activity, and explain
353 PTV's limited activity against HHV3.

354 **Discussion**

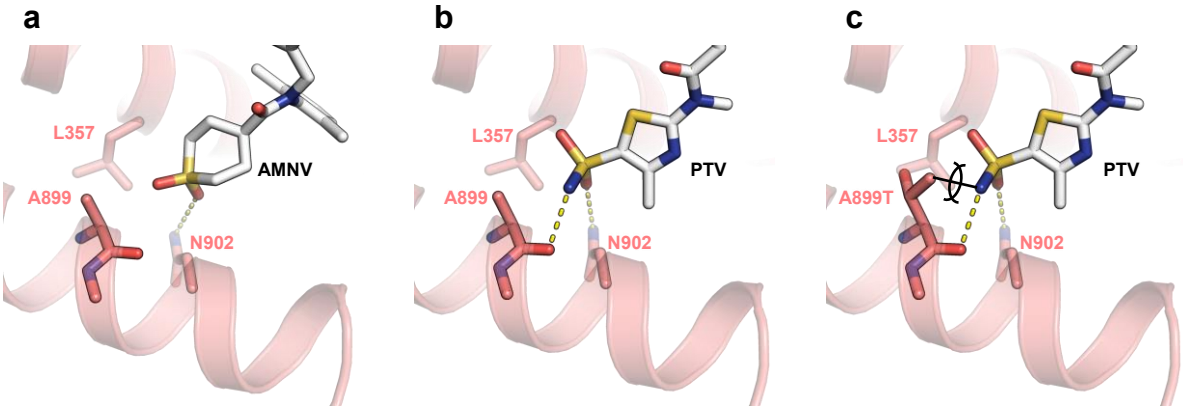

Figure S11: A potential effect of UL52 A899 substitutions on PTV binding, but not AMNV, related to Figure 4. a, A hydrogen bond between the sulfonyl group of AMNV and the side chain of N902. **b**, Two hydrogen bonds between the sulfonamide group of PTV and both the side chain of N902 and the carbonyl group of A899. **c**, A structural model of the A899T substitution, which confers resistance to PTV. The Cγ atom of A899T is positioned too close to the amino group of PTV.

355 Our structural, biochemical, and computational analyses collectively elucidate the
356 mechanism of action of AMNV and PTV and shed light on why these HPIs are less
357 effective against the β- and γ-herpesvirus subfamilies. Moreover, our MD and FMO
358 analyses clarify how a small difference in the chemical structures of AMNV and PTV
359 results in distinct anti-herpesvirus spectra within the α-subfamily. Together, these findings
360 establish a structural framework for the rational design of novel HPIs with tailored anti-
361 herpesvirus spectrum and/or improved pharmacokinetic properties.

362 Structures solved by cryo-EM often lack information on conformational dynamics, and may
363 suffer from limited resolution, leading to uncertainty in positioning of ligands and
364 surrounding water molecules. To overcome these limitations, we performed molecular
365 dynamics (MD) simulations to capture structural fluctuations and water behavior, followed
366 by FMO analysis to quantitatively evaluate molecular interactions. This integrated
367 approach provided in-depth insights into HPI–HPC interactions that aligned well with
368 previous mutational studies, supporting the reliability of our methodology. The combined
369 use of MD and FMO thus represents a powerful framework for investigating systems where
370 structural data alone is insufficient to fully characterize essential molecular interactions[41,42].

371 Helicases, which play essential roles in nearly all aspects of nucleic acid metabolism, have
372 long been recognized as promising drug targets. However, developing effective helicase
373 inhibitors has proven challenging, likely due to the chemical nature of the ATP- and nucleic
374 acid-binding sites, which are difficult to target with small molecules[43,44]. Recent studies
375 have reported the development of specific helicase inhibitors that act allosterically[45–47]. In

this study, we demonstrate that AMNV and PTV, two clinical inhibitors, bind to a shared allosteric pocket at the interface between the helicase subunit (UL5) and the non-helicase subunit (UL52). Our detailed characterization of these clinical HPIs, which act allosterically yet competitively, provides valuable insights for the development of diverse inhibitors targeting helicases from a wide range of sources, including both cellular and pathogenic origins.

The current HPC structures shed light on the coupling mechanism between DNA unwinding and primer synthesis; however, several questions remain unresolved. Do UL5 and UL52 engage with a single continuous ssDNA strand? How do the HM and PM reposition themselves during the catalytic cycle? Does the ZBD participate in binding the ssDNA template to facilitate efficient primer synthesis by the PD? To address these questions and elucidate the coupling mechanism, it will be necessary to determine the structures of HPC actively engaged in both DNA unwinding and primer synthesis in both ATP-bound and ATP-free states. Such structural insights will also be valuable for deepening our understanding of DNA replication mechanisms across diverse organisms.

Resource availability

Lead contact

Further information and requests for resources and reagents should be directed to and will be fulfilled by the lead contact, Toru Sengoku (tsengoku@yokohama-cu.ac.jp).

396 **Materials availability**

397 Plasmids generated in this study are available from the lead contact upon request.

398 **Data and code availability**

399 Coordinates and density maps have been deposited in Protein Data Bank (accession codes
400 9UT1, 9UT3, 9UT4, 9UT5, 9UT6, and 9UT7) and Electron Microscopy Data Bank
401 (accession codes EMD-64478, EMD-64479, EMD-64480, EMD-64481, EMD-64482, and
402 EMD-64483), respectively. All structure files and a set of input/output files used for FMO
403 calculations are available at the FMODB (https://drugdesign.riken.jp/FMODB/)[48] The
404 FMODBIDs for the representative structures of AMNV-HP complex in clusters 0-3 are
405 YJ552, 5817Z, 4812N, and KM4Y3, respectively. The FMODBIDs for the representative
406 structures of PTV-HP complex in clusters 0-3 are QJ2RY, RV7Z8, Z14JN, and 681MZ,
407 respectively. Simple data analysis can be performed using the FMODB web interface, and
408 detailed analysis can be performed using the BioStation Viewer software
409 (https://fmodd.jp/biostationviewer-dl/).

410

411 **Acknowledgements**

412 We thank members of Nureki Laboratory for their support in cryo-EM data collection. MD
413 calculations were performed using computational resources of the supercomputer system
414 (HPE SGI8600) jointly operated by the Japan Atomic Energy Agency (JAEA) and the
415 National Institutes for Quantum Science and Technology (QST). FMO calculations were

performed as part of the activities of the FMO Drug Design Consortium (FMODD) using the supercomputer “Fugaku” at RIKEN (project ID: hp240162).

This work was supported by JSPS KAKENHI (grant number 25K02501), Sumitomo Foundation, Shionogi Infectious Disease Research Promotion Foundation, and Uehara Memorial Foundation to T.S. This research was also partially supported by Research Support Project for Life Science and Drug Discovery (Basis for Supporting Innovative Drug Discovery and Life Science Research (BINDS)) from Japan Agency for Medical Research and Development (AMED) under grant numbers JP25ama121012 (support No. 6021) to O.N., JP25ama121024 (support No. 5660) to H.K., and JP25ama121030 (Support No. 5726) to K.F.

Author contributions

K.S. purified proteins, collected the cryo-EM data, solved the structures, performed biochemical experiments, analyzed data, and wrote the paper. H.I. and H.K. performed MD simulations and wrote the paper. T.M. and K.F. performed FMO analysis and wrote the paper. S.K. purified proteins and performed biochemical experiments. Y.K., K.H., and O.N. assisted with cryo-EM data collection. C.O. and A.O. purified proteins. T.S. designed the project, solved the structures, analyzed data, and wrote the paper.

Declaration of interests

The authors declare no competing interests.

Declaration of Generative AI and AI-assisted technologies in the writing process

During the preparation of this work the author used ChatGPT in order to improve readability and language. After using this service, the authors reviewed and edited the content as needed and take full responsibility for the content of the publication.

Figure legends

Figure 1: Overall structure of the AMNV-bound HPC from HHV1. a, Domain architectures of the three subunits and their interactions with each other and with ssDNA. The color scheme used in this panel is applied consistently throughout the paper to distinguish different domains. b, A cartoon illustration of the HPC. c, 3DFlex map (calculated using 3DFlex) and the ribbon model of the AMNV-bound HPC. See also Figure S1-S8 and Table S1-S2.

Figure 2: UL5-DNA interaction. a, The bound ssDNA is wrapped by domains 1A, 2A, and 2B (two views). UL5 and ssDNA are shown as a transparent surface model and a sphere model, respectively. b, Schematic representation of ssDNA-UL5 interaction. c, Two structural motifs interfering with base-stacking interactions. d and e, Interactions between ssDNA and domain 1A (d) or domain 2A (e).

455 Figure 3: HPIs may lock UL5 in an open conformation. a-c, Structures of domains 1A and
456 2A in the ssDNA-bound states of the AMNV-bound HPC (a), ADP-bound Pif1 (b), and ATP
457 analog-bound Pif1 (c). DNA nucleotides contacted by conserved residues in motifs Ia and
458 IV (T122 and S397 of UL5 and their equivalents) are labeled. d-f, Close-up views of the
459 ATPase site in the AMNV-bound HPC (d), ADP-bound Pif1 (e), and ATP analog-bound
460 Pif1 (f). g, h, Relationship between ATP concentration and apparent inhibition constant
461 (Kiapp), along with their standard error of the mean (SEM), in ATPase inhibition assays of
462 AMNV (g) and PTV (h). The corresponding Ki and α values with SEM are also shown. i,
463 Distribution of the distance between the centers of mass of K103, D249, and E250 in
464 domain 1A and R841 in domain 2A during MD simulations. j, Proposed model for the
465 inhibition mechanism of HPIs. See also Figure S9 and S10.

466 Figure 4: Binding and specificity of HPIs. a, Overall structure of the HPC, with the HPI
467 binding site highlighted by a box. b, c, Stereo views of the binding site for AMNV (b) and
468 PTV (c). Residues associated with resistance mutations are underlined. d, Sequence
469 alignment of residues involved in HPI binding. “A” and “P” denote mutations that confer
470 resistance to AMNV and PTV, respectively. e, Fragmentation scheme used for FMO
471 calculations. f–i, PIEDA results showing interactions between AMNV and UL5 (f), AMNV
472 and UL52 (g), PTV and UL5 (h), and PTV and UL52 (i). ES, EX, CT, and DI refer to the
473 electrostatic, exchange-repulsion, charge transfer with higher-order mixing, and dispersion
474 terms, respectively. Asterisks indicate residues contributing more than 5 kcal/mol to
475 binding in one complex compared to the other. j, k, Schematic representations of the
476 interactions between the HPC and AMNV (j) or PTV (k). See also Figure S11.

477

478 **Methods**

479 **Experimental model and study participant details**

480 **Cell lines**

481 Spodoptera frugiperda (Sf9) insect cells were cultured and maintained in Sf-900 II SFM
482 insect cell culture medium (Thermo Fisher Scientific) at 27 °C.

483 **Methods details**

484 **Protein expression and purification**

485 Full-length coding sequences of HHV-1 UL5, UL52, and UL8 were synthesized by Twist
486 Bioscience and individually cloned into the pACEBac1 vector. An N-terminal twin-strep–
487 His tag was fused to UL5, while N-terminal His–SUMOstar tags were fused to UL52 and
488 UL8. Baculoviruses were generated in Sf9 cells using the Bac-to-Bac system (Thermo
489 Fisher Scientific) according to the manufacturer's protocol. The HPC was reconstituted by
490 co-infecting Sf9 cells with the three respective recombinant baculoviruses at a multiplicity
491 of infection of 3:3:3. Cells were harvested 48 hours post-infection.

492 Cell pellets were resuspended in lysis buffer (100 mM Tris-HCl (pH 8.0), 150 mM NaCl,
493 1 mM $MgCl_2$, 0.5 mM TCEP, 0.5% Tween 20, 10% glycerol, 0.1 mM PMSF, and cOmplete
494 ULTRA protease inhibitor cocktail (Roche)) and lysed by sonication. The clarified lysate
495 was loaded onto a Strep-Tactin XT 4Flow column (IBA Lifesciences), and the bound
496 protein complex was eluted with buffer containing 20 mM Tris-HCl (pH 8.0), 500 mM

497 NaCl, 10% glycerol, 0.5 mM TCEP, and 50 mM D-biotin. The eluate was subsequently
498 applied to a HisTrap HP column (Cytiva) and eluted with buffer containing 20 mM Tris-
499 HCl (pH 8.0), 500 mM NaCl, 10% glycerol, 0.5 mM TCEP, and 500 mM imidazole. The
500 eluted sample was dialyzed against buffer A (20 mM Tris-HCl (pH 8.0), 150 mM NaCl,
501 0.5 mM TCEP) and concentrated for cryo-EM sample preparation.

502 For tag removal, the HisTrap eluate was mixed with SUMOstar protease and HRV 3C
503 protease and dialyzed against buffer A. The sample was subsequently passed through a
504 HisTrap column to remove cleaved tags and proteases. The flow-through containing tag-
505 free HPC was further dialyzed against buffer A, concentrated, flash-frozen in liquid
506 nitrogen, and stored at −80 °C for ATPase assays.

507 **Cryo-EM sample preparation**

508 For grid preparation of the AMNV-bound complex, 0.4 μM tagged HPC was mixed with 4
509 μM 43-mer ssDNA (5'-TTTTTTTTTCCTGTTTTTTTTTTTTTTTTTTTTTTTTTTTTTTT-
510 3'; Fasmac), 1 mM AMP-PNP, 10 mM $MgCl_2$, and 100 μM AMNV (AstaTech), and then
511 concentrated 10-fold. For the PTV-bound complex, 0.48 μM tagged HPC was mixed with
512 4.8 μM 43-mer ssDNA, 1 mM AMP-PNP, 10 mM $MgCl_2$, and 100 μM PTV (Selleck), and
513 then concentrated 7.6-fold. Concentration was performed using a Vivaspin 500 device
514 (MWCO 50 kDa; Sartorius).

515 Due to orientation bias observed on Au 300-mesh R1.2/1.3 grids, the samples were applied
516 to freshly glow-discharged Au 300-mesh R0.6/1 holey carbon grids (Quantifoil), pre-treated
517 with 3 μL of amylamine to mitigate bias[49]. The grids were blotted for 4 s at 4 °C under

518 100% humidity and plunge-frozen in liquid ethane using a Vitrobot Mark IV (Thermo
519 Fisher Scientific).

520 **Cryo-EM data acquisition and processing**

521 Cryo-EM data were collected using a Titan Krios G4 transmission electron microscope
522 (Thermo Fisher Scientific) operated at 300 kV, equipped with a K3 direct electron detector
523 (Gatan), installed at the University of Tokyo. Data acquisition was performed using EPU
524 v3.4.0.5704, with a defocus range of −0.6 to −1.6 μm. Data acquisition statistics are
525 summarized in Supplementary Table 1.

526 The cryo-EM data were processed using CryoSPARC v4.4.1[50] (Figures S1 and S2). For the
527 AMNV complex, an initial dataset of 803 micrographs was used for blob picking, 2D
528 classification, and template generation. These templates were then applied to the main
529 dataset of 12,466 micrographs for template-based particle picking, followed by neural
530 network-based picking using Topaz[51]. Subsequent reconstruction and refinement yielded a
531 global map with poorly resolved density in the HM. Following 3D classification without a
532 focus mask, seven out of ten classes were selected, which showed slightly improved HM
533 density. Particles corresponding to the HM and PM were then subtracted and used for local
534 refinement. The global map was further refined using 3DFlex[16].

535 For the PTV complex, data were processed similarly to the AMNV dataset. However, the
536 AMNV-derived templates were reused for template-based particle picking, and no particle
537 subtraction was performed.

538 **Model building and refinement**

539 The initial model of the HPC was generated using LocalColabFold[52], which employs
540 AlphaFold2[53] for structure prediction, and was fitted into the cryo-EM map. The predicted
541 model showed good overall agreement with the map, although notable differences were
542 observed in local loop regions (including the HPIs binding pocket) and in the relative
543 orientation between the HM and PM. The model was manually adjusted using Coot
544 v0.9.8.93[54] and further refined with the *phenix.real_space_refine* module in Phenix
545 v1.21.1-5286[55]. No map sharpening was applied. To build the atomic models of the HPIs,
546 multiple conformations of their functional groups (the oxadiazole ring of AMNV, and the
547 pyridine ring and NH_2 group of PTV) were generated and evaluated using FMO
548 calculations. The conformation with the lowest energy was then selected. Structural figures
549 were prepared using PyMOL v2.5.0 (Schrödinger, LLC) and ChimeraX v1.9[56]. Data
550 processing and refinement statistics are summarized in Supplementary Table 2.

551 **ATPase assay**

552 ATPase activity was assessed using an NADH-coupled microplate assay as previously
553 described[57], performed over a 30-minute time course at 30 °C, with absorbance
554 measurements taken every 30 seconds. Each 54 µL reaction was prepared in ATPase buffer
555 containing 20 mM HEPES-NaOH (pH 7.5), 5 mM $MgCl_2$, 10% glycerol, 5 mM TCEP,
556 100 µg/mL bovine serum albumin, 2 µM 43-mer ssDNA, 3 mM phosphoenolpyruvate
557 (Nacalai Tesque), 1 mM NADH (Sigma-Aldrich), 1% DMSO, 0.02 U/µL L-lactate
558 dehydrogenase (Sigma-Aldrich), 0.02 U/µL pyruvate kinase (Sigma-Aldrich), 10 nM tag-
559 free HPC, and ATP (Nacalai Tesque) at final concentrations of 0, 0.1, 0.2, 0.3, 0.7, 1.5, or

560 3 mM. Either AMNV or PTV was added separately at concentrations of 0, 2.5, 5, 10, 15,
561 20, or 25 nM. Reactions were dispensed into a 96-well half-area microplate (Greiner Bio-
562 One), and NADH oxidation was monitored by measuring absorbance at 340 nm using a
563 Tecan Spark Cyto 400 multimode microplate reader. Reaction velocities (v, OD/sec) were
564 determined from the linear portion of the absorbance decrease at 340 nm between 1000 and
565 1500 seconds. Background signals measured in the absence of ATP were subtracted to
566 correct the data. The Michaelis constant (K_M) was determined by non-linear fitting to the
567 Michaelis–Menten equation using GraphPad Prism v10.2.3 (GraphPad Software).

568 Both AMNV and PTV exhibited EC_{50} values of less than 100 nM against the virus [12,14],
569 indicating their behavior as tight-binding inhibitors [32,58]. The apparent inhibition constant
570 (K_i^{app}) was determined by non-linear fitting to the Morrison equation (Eq. 1), where v_i is the
571 initial rate of the inhibited reaction, v_0 is the initial rate of the uninhibited reaction, [E] is
572 the enzyme concentration, [I] is the inhibitor concentration, and K_i^{app} is the apparent
573 inhibition constant [32,58].

574 $$v_i = v_0\left(1 - \frac{([E]+[I]+K_i^{app}) - \sqrt{([E]+[I]+K_i^{app})^2 - 4[E][I]}}{2[E]}\right) \qquad \text{(Eq. 1)}$$

575 The K_i^{app} values were plotted against ATP concentrations and fitted by non-linear regression
576 to a mixed inhibition model (Eq. 2), in which [S] represents the ATP concentration, K_M is
577 the Michaelis constant, α reflects the difference in inhibitor affinity for the free enzyme
578 versus the enzyme-substrate complex, and K_i is the inhibition constant [32,58]. This analysis
579 yielded values for α and K_i.

580 $$K_{\mathrm{i}}^{\mathrm{app}} = \frac{[\mathrm{S}]+K_{\mathrm{M}}}{\frac{K_{\mathrm{M}}}{K_{\mathrm{i}}}+\frac{[\mathrm{S}]}{\alpha K_{\mathrm{i}}}} \quad \text{(Eq. 2)}$$

581 **Modeling of the UL5–UL52 subcomplex for MD simulations**

582 For UL5, the N-terminal region (M1–A33) and a large C-terminal loop (A582–E657) were
583 excluded from the model. A shorter missing loop (A563–E568) was modeled using
584 MODELLER[59], and the termini adjacent to the large loop (T581, T658) were capped with
585 N-methylamide (NME) and acetyl (ACE) groups, respectively. For UL52, the N- and C-
586 terminal regions (M1–T16, P1044–P1058), as well as a large internal loop (P682–P752),
587 were also excluded. The termini flanking this large loop (R681, V753) were capped in the
588 same manner. Three smaller loops (S170–D183, P481–C498, R995–A996) were modeled
589 with MODELLER by generating 100 loop conformations with the remaining structure held
590 fixed; the lowest-energy models were selected for each. The resulting structure was used
591 for subsequent molecular dynamics simulations.

592 **MD simulations of the UL5–UL52 subcomplexes**

593 We prepared four systems of the UL5–UL52 complex: two containing ligands (AMNV or
594 PTV) and two ligand-free systems generated by removing the respective ligands. MD
595 simulations were performed using the pmemd module in AMBER20[60,61], with force fields
596 ff99SB for protein[62], bsc1 for DNA[63], and ff99ions08 for ions[64]. The force field parameters
597 for ligands were prepared using the Antechamber package[65] in AmberTools and the general
598 Amber force field (GAFF)[66] for organic molecules. A quantum chemical calculation to
599 geometrically optimize the ligands were carried out with HF/6-31G* basis set using

600 Gaussian 03 software[67]. The net charge for each ligand was set at 0. Discrete partial atomic
601 charges were assigned with HF/6-31G* basis set using the Restrained Electrostatic
602 Potential (RESP) fitting method[68]. The zinc AMBER force field (ZAFF) for the 4-
603 coordinated zinc metal centers[69] was used for the zinc ion in the ZBD. The UL5 – UL52
604 complex was solvated in a cubic periodic box of ~ 190 Å × 190 Å × 190 Å , containing ~
605 220,000 TIP3P water molecules[70] and 0.15 M NaCl to mimic physiological ionic strength.
606 The complex was positioned such that all atoms were separated at least 20 Å from the edge
607 of the box. The resulting system contained ~ 690,000 atoms in total.

608 For each of the four systems, the MD simulations were carried out using eight replicas of
609 identical structures, each initiated with different random seeds for velocity assignment.
610 Each replica was run for 3.16 μs, totaling 25.28 μs per system, under constant pressure of
611 one bar and temperature of 300 K. The dielectric constant was set to 1.0 and the van der
612 Waals interactions were calculated with a 9 Å cutoff. Electrostatic interactions were treated
613 using the particle mesh Ewald (PME) method[71], with a charge grid spacing close to 1 Å.
614 The charge grid was interpolated using a fourth-order cubic B-spline with the direct sum
615 tolerance of 10^{-5} at a 9 Å direct space cutoff. Temperature and pressure were regulated by
616 Langevin dynamics with a collision frequency of 2 ps^{-1}; coupling times were set to 1 ps^{-1}
617 for both. Bond lengths involving hydrogen atoms were constrained with the SHAKE
618 algorithm[72,73]. The leap-frog algorithm was used to integrate the equations of motion with a
619 2 fs time step. The system was gradually heated from 0 K to 300 K over 10 ns, during
620 which the solute atoms were restrained with decreasing force constants while water
621 molecules and ions were allowed to move freely. Conformational snapshots were saved

every 100 ps. Trajectories from the final 3 μs of each of the eight replicas (totaling 24 μs) were used for analysis. Water density maps were generated using the volmap tool in VMD[74].

K-mean clustering of the MD trajectories

K-means clustering was performed on all atoms in residues located within 3.5 Å of the ligands in the energy-minimized structure. Specifically, these residues were Asn98, Ile341, Asn343, Met355, Lys356, Glu359, Tyr836, and Tyr882 of UL5, and Tyr356, Phe360, Ala899, and Asn902 of UL52. K-means clustering with K = 4 grouped the trajectories for the UL5-UL52 complex with AMNV into four distinct clusters: 10.5%, 40.2%, 42.7%, and 6.6% of the total trajectory. For the PTV-bound complex, the corresponding cluster populations were 70.0%, 4.9%, 0.1%, and 25.0%. Representative structures were selected as those closest to the centroids of each cluster. The RMSD values relative to the centroids were 0.659, 0.515, 0.588, and 0.703 Å for the AMNV-bound UL5–UL52 complex, and 0.568, 0.555, 0.779, and 0.520 Å for the PTV-bound complex.

FMO calculation and interaction energy analysis

FMO calculations were performed on the representative structures obtained by clustering of MD trajectories. As a preprocessing step, MD representative structures were subjected to energy minimization by applying a positional constraint of 1.0 kcal/mol-Å^2 to heavy atoms, and water within 10 Å around the HPC protein, HPI, ssDNA, and ligand was extracted for calculation. Fragmentation was performed by using amino acid residue units for proteins, base and sugar-phosphate fragments for DNA, and single fragments for ligand and water

643 molecules[75]. The FMO calculations were performed at the MP2/6-31G*[76,77] theoretical
644 level using the ABINIT-MP program[78]. The supercomputer Fugaku was used.

645 Defining the inter-fragment interaction energy (IFIE) between fragments i and j as E_{ij}, pair
646 interaction energy decomposition analysis (PIEDA)[40] divides IFIE into four energy
647 components as follows.

648 $E_{ij} = E_{ij}^{ES} + E_{ij}^{EX} + E_{ij}^{CT+mix} + E_{ij}^{DI}$ (Eq 3)

649 In this study, *i* is HPI (AMNV or PTV), and *j* is each residue of HPC. Weighted average
650 IFIE/PIEDA, E_{ij}^{weight}, is the sum of the interaction energies between HPI and each residue
651 in the cluster representative structure, weighted by the occurrence frequency of each cluster.

652 $E_{ij}^{weight} = \sum_{\alpha} w_{\alpha} E_{ij}^{\alpha}$ (Eq.4)

653 Here, w_{α} is the weight of cluster α, which is 0.105, 0.402, 0.427, and 0.066 for AMNV, and
654 0.700, 0.049, 0.001, and 0.250 for PTV. Figure 4f-i shows the weighted average interaction
655 energy calculated using Eq. 4.

656 Cryo-EM structures were also evaluated using MP2/6-31G* level FMO calculations. For
657 preprocessing of the structures, hydrogen atoms were added and energy minimization was
658 performed using Amber10:EHT force field.

659 **QUANTIFICATION AND STATISTICAL ANALYSIS**

660 Cryo-EM data collection and refinement statistics are summarized in Table S1.

661

662 **Supplemental Information**

663 Document S1. Figures S1-S11, Tables S1, and S2.

664 Video S1. Overall structure of the AMNV-bound complex.

665 Video S2. AMNV binding site.

666

667 **References**

668 1. Arvin, A.M. ed. (2007). Human herpesviruses: biology, therapy, and
669 immunoprophylaxis (Cambridge University Press).

670 2. Marcocci, M.E., Napoletani, G., Protto, V., Kolesova, O., Piacentini, R., Li Puma,
671 D.D., Lomonte, P., Grassi, C., Palamara, A.T., and De Chiara, G. (2020). Herpes
672 Simplex Virus-1 in the Brain: The Dark Side of a Sneaky Infection. Trends Microbiol.
673 *28*, 808–820. https://doi.org/10.1016/j.tim.2020.03.003.

674 3. Eyting, M., Xie, M., Michalik, F., Heß, S., Chung, S., and Geldsetzer, P. (2025). A
675 natural experiment on the effect of herpes zoster vaccination on dementia.
676 Nature, 1–9. https://doi.org/10.1038/s41586-025-08800-x.

677 4. Bjornevik, K., Münz, C., Cohen, J.I., and Ascherio, A. (2023). Epstein–Barr virus as a
678 leading cause of multiple sclerosis: mechanisms and implications. Nat. Rev.
679 Neurol. *19*, 160–171. https://doi.org/10.1038/s41582-023-00775-5.

680 5. Mozhgani, S.-H., Rajabi, F., Qurbani, M., Erfani, Y., Yaslianifard, S., Moosavi, A.,
681 Pourrostami, K., Baradaran Bagheri, A., Soleimani, A., Behzadian, F., et al. (2021).
682 Human Herpesvirus 6 Infection and Risk of Chronic Fatigue Syndrome: A
683 Systematic Review and Meta-Analysis. Intervirology *65*, 49–57.
684 https://doi.org/10.1159/000517930.

685 6. Bermek, O., and Williams, R.S. (2021). The three-component helicase/primase
686 complex of herpes simplex virus-1. Open Biol. *11*, 210011.
687 https://doi.org/10.1098/rsob.210011.

7. Fernandez, A.J., and and Berger, J.M. (2021). Mechanisms of hexameric helicases. Crit. Rev. Biochem. Mol. Biol. *56*, 621–639. https://doi.org/10.1080/10409238.2021.1954597.

8. Fairman-Williams, M.E., Guenther, U.-P., and Jankowsky, E. (2010). SF1 and SF2 helicases: family matters. Curr. Opin. Struct. Biol. *20*, 313–324. https://doi.org/10.1016/j.sbi.2010.03.011.

9. Saikrishnan, K., Powell, B., Cook, N.J., Webb, M.R., and Wigley, D.B. (2009). Mechanistic Basis of 5'-3' Translocation in SF1B Helicases. Cell *137*, 849–859. https://doi.org/10.1016/j.cell.2009.03.036.

10. Bergsch, J., Allain, F.H.-T., and Lipps, G. (2019). Recent advances in understanding bacterial and archaeoeukaryotic primases. Curr. Opin. Struct. Biol. *59*, 159–167. https://doi.org/10.1016/j.sbi.2019.08.004.

11. Shiraki, K., Yasumoto, S., Toyama, N., and Fukuda, H. (2021). Amenamevir, a Helicase-Primase Inhibitor, for the Optimal Treatment of Herpes Zoster. Viruses *13*, 1547. https://doi.org/10.3390/v13081547.

12. Chono, K., Katsumata, K., Kontani, T., Kobayashi, M., Sudo, K., Yokota, T., Konno, K., Shimizu, Y., and Suzuki, H. (2010). ASP2151, a novel helicase-primase inhibitor, possesses antiviral activity against varicella-zoster virus and herpes simplex virus types 1 and 2. J. Antimicrob. Chemother. *65*, 1733–1741. https://doi.org/10.1093/jac/dkq198.

13. Ohtsu, Y., Susaki, Y., and Noguchi, K. (2018). Absorption, Distribution, Metabolism, and Excretion of the Novel Helicase-Primase Inhibitor, Amenamevir (ASP2151), in Rodents. Eur. J. Drug Metab. Pharmacokinet. *43*, 693–706. https://doi.org/10.1007/s13318-018-0481-y.

14. Kleymann, G., Fischer, R., Betz, U.A.K., Hendrix, M., Bender, W., Schneider, U., Handke, G., Eckenberg, P., Hewlett, G., Pevzner, V., et al. (2002). New helicase-primase inhibitors as drug candidates for the treatment of herpes simplex disease. Nat. Med. *8*, 392–398. https://doi.org/10.1038/nm0402-392.

15. Birkmann, A., Bonsmann, S., Kropeit, D., Pfaff, T., Rangaraju, M., Sumner, M., Timmler, B., Zimmermann, H., Buschmann, H., and Ruebsamen-Schaeff, H. (2022). Discovery, Chemistry, and Preclinical Development of Pritelivir, a Novel Treatment Option for Acyclovir-Resistant Herpes Simplex Virus Infections. J. Med. Chem. *65*, 13614–13628. https://doi.org/10.1021/acs.jmedchem.2c00668.

16. Punjani, A., and Fleet, D.J. (2023). 3DFlex: determining structure and motion of flexible proteins from cryo-EM. Nat. Methods *20*, 860–870. https://doi.org/10.1038/s41592-023-01853-8.

17. Holm, L., Laiho, A., Törönen, P., and Salgado, M. (2023). DALI shines a light on remote homologs: One hundred discoveries. Protein Sci. *32*, e4519. https://doi.org/10.1002/pro.4519.

18. Chen, W.-F., Dai, Y.-X., Duan, X.-L., Liu, N.-N., Shi, W., Li, N., Li, M., Dou, S.-X., Dong, Y.-H., Rety, S., et al. (2016). Crystal structures of the BsPif1 helicase reveal that a major movement of the 2B SH3 domain is required for DNA unwinding. Nucleic Acids Res. *44*, 2949–2961. https://doi.org/10.1093/nar/gkw033.

19. Zhou, X., Ren, W., Bharath, S.R., Tang, X., He, Y., Chen, C., Liu, Z., Li, D., and Song, H. (2016). Structural and Functional Insights into the Unwinding Mechanism of *Bacteroides sp* Pif1. Cell Rep. *14*, 2030–2039. https://doi.org/10.1016/j.celrep.2016.02.008.

20. Dai, Y.-X., Chen, W.-F., Liu, N.-N., Teng, F.-Y., Guo, H.-L., Hou, X.-M., Dou, S.-X., Rety, S., and Xi, X.-G. (2021). Structural and functional studies of SF1B Pif1 from *Thermus oshimai* reveal dimerization-induced helicase inhibition. Nucleic Acids Res. *49*, 4129–4143. https://doi.org/10.1093/nar/gkab188.

21. Lu, K.-Y., Xin, B.-G., Zhang, T., Liu, N.-N., Li, D., Rety, S., and Xi, X.-G. (2021). Structural study of the function of *Candida Albicans* Pif1. Biochem. Biophys. Res. Commun. *567*, 190–194. https://doi.org/10.1016/j.bbrc.2021.06.050.

22. Velankar, S.S., Soultanas, P., Dillingham, M.S., Subramanya, H.S., and Wigley, D.B. (1999). Crystal Structures of Complexes of PcrA DNA Helicase with a DNA Substrate Indicate an Inchworm Mechanism. Cell *97*, 75–84. https://doi.org/10.1016/S0092-8674(00)80716-3.

23. Li, A.W.H., Zabrady, K., Bainbridge, L.J., Zabrady, M., Naseem-Khan, S., Berger, M.B., Kolesar, P., Cisneros, G.A., and Doherty, A.J. (2022). Molecular basis for the initiation of DNA primer synthesis. Nature *605*, 767–773. https://doi.org/10.1038/s41586-022-04695-0.

24. Chen, Y., Bai, P., Mackay, S., Korza, G., Carson, J.H., Kuchta, R.D., and Weller, S.K. (2011). Herpes Simplex Virus Type 1 Helicase-Primase: DNA Binding and Consequent Protein Oligomerization and Primase Activation. J. Virol. *85*, 968–978. https://doi.org/10.1128/JVI.01690-10.

25. David, A., Islam, S., Tankhilevich, E., and Sternberg, M.J.E. (2022). The AlphaFold Database of Protein Structures: A Biologist's Guide. J. Mol. Biol. *434*, 167336. https://doi.org/10.1016/j.jmb.2021.167336.

26. Keen, B.A., Jozwiakowski, S.K., Bailey, L.J., Bianchi, J., and Doherty, A.J. (2014). Molecular dissection of the domain architecture and catalytic activities of human PrimPol. Nucleic Acids Res. *42*, 5830–5845. https://doi.org/10.1093/nar/gku214.

27. Kazlauskas, D., and Venclovas, Č. (2014). Herpesviral helicase-primase subunit UL8 is inactivated B-family polymerase. Bioinformatics *30*, 2093–2097. https://doi.org/10.1093/bioinformatics/btu204.

28. Muylaert, I., Zhao, Z., Andersson, T., and Elias, P. (2012). Identification of Conserved Amino Acids in the Herpes Simplex Virus Type 1 UL8 Protein Required for DNA Synthesis and UL52 Primase Interaction in the Virus Replisome *. J. Biol. Chem. *287*, 33142–33152. https://doi.org/10.1074/jbc.M112.356782.

29. Zhu, L.A., and Weller, S.K. (1992). The six conserved helicase motifs of the UL5 gene product, a component of the herpes simplex virus type 1 helicase-primase, are essential for its function. J. Virol. *66*, 469–479. https://doi.org/10.1128/jvi.66.1.469-479.1992.

30. Graves-Woodward, K.L., Gottlieb, J., Challberg, M.D., and Weller, S.K. (1997). Biochemical Analyses of Mutations in the HSV-1 Helicase-Primase That Alter ATP Hydrolysis, DNA Unwinding, and Coupling Between Hydrolysis and Unwinding. J. Biol. Chem. *272*, 4623–4630. https://doi.org/10.1074/jbc.272.7.4623.

31. Soultanas, P., Dillingham, M.S., Velankar, S.S., and Wigley, D.B. (1999). DNA binding mediates conformational changes and metal ion coordination in the active site of PcrA helicase1. J. Mol. Biol. *290*, 137–148. https://doi.org/10.1006/jmbi.1999.2873.

32. Copeland, R.A. (2000). Enzymes: A Practical Introduction to Structure, Mechanism, and Data Analysis 1st ed. (Wiley) https://doi.org/10.1002/0471220639.

33. Sato, Y., Suenaga, T., Kobayashi, M., Miyazaki, N., Suzuki, T., Ishioka, K., and Suzutani, T. (2021). Characteristics of Helicase-Primase Inhibitor Amenamevir-Resistant Herpes Simplex Virus. Antimicrob. Agents Chemother. *65*, e00494-21. https://doi.org/10.1128/AAC.00494-21.

34. Biswas, S., Miguel, R.N., Sukla, S., and Field, H.J. (2009). A mutation in helicase motif IV of herpes simplex virus type 1 UL5 that results in reduced growth in vitro

and lower virulence in a murine infection model is related to the predicted helicase structure. J. Gen. Virol. *90*, 1937–1942. https://doi.org/10.1099/vir.0.011221-0.

35. Biswas, S., Kleymann, G., Swift, M., Tiley, L.S., Lyall, J., Aguirre-Hernández, J., and Field, H.J. (2008). A single drug-resistance mutation in HSV-1 UL52 primase points to a difference between two helicase–primase inhibitors in their mode of interaction with the antiviral target. J. Antimicrob. Chemother. *61*, 1044–1047. https://doi.org/10.1093/jac/dkn057.

36. Fedorov, D.G., Nagata, T., and Kitaura, K. (2012). Exploring chemistry with the fragment molecular orbital method. Phys. Chem. Chem. Phys. *14*, 7562. https://doi.org/10.1039/c2cp23784a.

37. Kitaura, K., Ikeo, E., Asada, T., Nakano, T., and Uebayasi, M. (1999). Fragment molecular orbital method: an approximate computational method for large molecules. Chem. Phys. Lett. *313*, 701–706. https://doi.org/10.1016/S0009-2614(99)00874-X.

38. Tanaka, S., Mochizuki, Y., Komeiji, Y., Okiyama, Y., and Fukuzawa, K. (2014). Electron-correlated fragment-molecular-orbital calculations for biomolecular and nano systems. Phys Chem Chem Phys *16*, 10310–10344. https://doi.org/10.1039/C4CP00316K.

39. Fukuzawa, K., and Tanaka, S. (2022). Fragment molecular orbital calculations for biomolecules. Curr. Opin. Struct. Biol. *72*, 127–134. https://doi.org/10.1016/j.sbi.2021.08.010.

40. Fedorov, D.G., and Kitaura, K. (2007). Pair interaction energy decomposition analysis. J. Comput. Chem. *28*, 222–237. https://doi.org/10.1002/jcc.20496.

41. Handa, Y., Okuwaki, K., Kawashima, Y., Hatada, R., Mochizuki, Y., Komeiji, Y., Tanaka, S., Furuishi, T., Yonemochi, E., Honma, T., et al. (2024). Prediction of Binding Pose and Affinity of Nelfinavir, a SARS-CoV-2 Main Protease Repositioned Drug, by Combining Docking, Molecular Dynamics, and Fragment Molecular Orbital Calculations. J. Phys. Chem. B *128*, 2249–2265. https://doi.org/10.1021/acs.jpcb.3c05564.

42. Saito, H., Handa, Y., Chen, M., Schneider-Poetsch, T., Shichino, Y., Takahashi, M., Romo, D., Yoshida, M., Fürstner, A., Ito, T., et al. (2024). DMDA-PatA mediates RNA sequence-selective translation repression by anchoring eIF4A and DDX3 to GNG motifs. Nat. Commun. *15*, 7418. https://doi.org/10.1038/s41467-024-51635-9.

43. Heuser, A., Abdul Rahman, W., Bechter, E., Blank, J., Buhr, S., Erdmann, D., Fontana, P., Mermet-Meillon, F., Meyerhofer, M., Strang, R., et al. (2024). Challenges for the Discovery of Non-Covalent WRN Helicase Inhibitors. ChemMedChem *19*, e202300613. https://doi.org/10.1002/cmdc.202300613.

44. Selvaratnam, L., Willson, T.M., and Schapira, M. (2025). Structural Chemistry of Helicase Inhibition. J. Med. Chem. *68*, 4022–4039. https://doi.org/10.1021/acs.jmedchem.4c01909.

45. Iwatani-Yoshihara, M., Ito, M., Klein, M.G., Yamamoto, T., Yonemori, K., Tanaka, T., Miwa, M., Morishita, D., Endo, S., Tjhen, R., et al. (2017). Discovery of Allosteric Inhibitors Targeting the Spliceosomal RNA Helicase Brr2. J. Med. Chem. *60*, 5759–5771. https://doi.org/10.1021/acs.jmedchem.7b00461.

46. Saalau-Bethell, S.M., Woodhead, A.J., Chessari, G., Carr, M.G., Coyle, J., Graham, B., Hiscock, S.D., Murray, C.W., Pathuri, P., Rich, S.J., et al. (2012). Discovery of an allosteric mechanism for the regulation of HCV NS3 protein function. Nat. Chem. Biol. *8*, 920–925. https://doi.org/10.1038/nchembio.1081.

47. Ferretti, S., Hamon, J., de Kanter, R., Scheufler, C., Andraos-Rey, R., Barbe, S., Bechter, E., Blank, J., Bordas, V., Dammassa, E., et al. (2024). Discovery of WRN inhibitor HRO761 with synthetic lethality in MSI cancers. Nature. https://doi.org/10.1038/s41586-024-07350-y.

48. Takaya, D., Watanabe, C., Nagase, S., Kamisaka, K., Okiyama, Y., Moriwaki, H., Yuki, H., Sato, T., Kurita, N., Yagi, Y., et al. (2021). FMODB: The World's First Database of Quantum Mechanical Calculations for Biomacromolecules Based on the Fragment Molecular Orbital Method. J. Chem. Inf. Model. *61*, 777–794. https://doi.org/10.1021/acs.jcim.0c01062.

49. Omura, S.N., and Nureki, O. (2025). Chapter Two - General and robust sample preparation strategies for cryo-EM studies of CRISPR-Cas9 and Cas12 enzymes. In Methods in Enzymology CRISPR-Cas Systems for RNA and Genome Editing - Part A., A. Ke and W. Tang, eds. (Academic Press), pp. 23–39. https://doi.org/10.1016/bs.mie.2025.01.052.

50. Punjani, A., Rubinstein, J.L., Fleet, D.J., and Brubaker, M.A. (2017). cryoSPARC: algorithms for rapid unsupervised cryo-EM structure determination. Nat. Methods *14*, 290–296. https://doi.org/10.1038/nmeth.4169.

51. Bepler, T., Morin, A., Rapp, M., Brasch, J., Shapiro, L., Noble, A.J., and Berger, B. (2019). Positive-unlabeled convolutional neural networks for particle picking in

cryo-electron micrographs. Nat. Methods *16*, 1153–1160. https://doi.org/10.1038/s41592-019-0575-8.

52. Mirdita, M., Schütze, K., Moriwaki, Y., Heo, L., Ovchinnikov, S., and Steinegger, M. (2022). ColabFold: making protein folding accessible to all. Nat. Methods *19*, 679–682. https://doi.org/10.1038/s41592-022-01488-1.

53. Jumper, J., Evans, R., Pritzel, A., Green, T., Figurnov, M., Ronneberger, O., Tunyasuvunakool, K., Bates, R., Žídek, A., Potapenko, A., et al. (2021). Highly accurate protein structure prediction with AlphaFold. Nature *596*, 583–589. https://doi.org/10.1038/s41586-021-03819-2.

54. Emsley, P., Lohkamp, B., Scott, W.G., and Cowtan, K. (2010). Features and development of *Coot*. Acta Crystallogr. D Biol. Crystallogr. *66*, 486–501. https://doi.org/10.1107/S0907444910007493.

55. Borbulevych, O.Y., Plumley, J.A., Martin, R.I., Merz, K.M., and Westerhoff, L.M. (2014). Accurate macromolecular crystallographic refinement: incorporation of the linear scaling, semiempirical quantum-mechanics program *DivCon* into the *PHENIX* refinement package. Acta Crystallogr. D Biol. Crystallogr. *70*, 1233–1247. https://doi.org/10.1107/S1399004714002260.

56. Pettersen, E.F., Goddard, T.D., Huang, C.C., Meng, E.C., Couch, G.S., Croll, T.I., Morris, J.H., and Ferrin, T.E. (2021). UCSF ChimeraX : Structure visualization for researchers, educators, and developers. Protein Sci. *30*, 70–82. https://doi.org/10.1002/pro.3943.

57. Kiianitsa, K., Solinger, J.A., and Heyer, W.-D. (2003). NADH-coupled microplate photometric assay for kinetic studies of ATP-hydrolyzing enzymes with low and high specific activities. Anal. Biochem. *321*, 266–271. https://doi.org/10.1016/S0003-2697(03)00461-5.

58. Reytor Gonzalez, M.L., and Alonso del Rivero Antigua, M. (2021). Reviewing the experimental and mathematical factors involved in tight binding inhibitors Ki values determination: The bi-functional protease inhibitor SmCI as a test model. Biochimie *181*, 86–95. https://doi.org/10.1016/j.biochi.2020.11.014.

59. Comparative Protein Structure Modeling of Genes and Genomes | Annual Reviews https://www.annualreviews.org/content/journals/10.1146/annurev.biophys.29.1.291.

60. Pearlman, D.A., Case, D.A., Caldwell, J.W., Ross, W.S., Cheatham, T.E., DeBolt, S., Ferguson, D., Seibel, G., and Kollman, P. (1995). AMBER, a package of computer

programs for applying molecular mechanics, normal mode analysis, molecular dynamics and free energy calculations to simulate the structural and energetic properties of molecules. Comput. Phys. Commun. *91*, 1–41. https://doi.org/10.1016/0010-4655(95)00041-D.

61. Case, D.A., K. Belfon, I.Y. Ben-Shalom, S.R. Brozell, D.S. Cerutti, T.E. Cheatham, III V.W.D. Cruzeiro, T.A. Darden, R.E. Duke, G. Giambasu, et al. (2020). Amber20. (Unpublished). https://doi.org/10.13140/RG.2.2.25321.36969 https://doi.org/10.13140/RG.2.2.25321.36969.

62. Hornak, V., Abel, R., Okur, A., Strockbine, B., Roitberg, A., and Simmerling, C. (2006). Comparison of multiple Amber force fields and development of improved protein backbone parameters. Proteins Struct. Funct. Bioinforma. *65*, 712–725. https://doi.org/10.1002/prot.21123.

63. Ivani, I., Dans, P.D., Noy, A., Pérez, A., Faustino, I., Hospital, A., Walther, J., Andrio, P., Goñi, R., Balaceanu, A., et al. (2016). Parmbsc1: a refined force field for DNA simulations. Nat. Methods *13*, 55–58. https://doi.org/10.1038/nmeth.3658.

64. Joung, I.S., and Cheatham, T.E. (2008). Determination of Alkali and Halide Monovalent Ion Parameters for Use in Explicitly Solvated Biomolecular Simulations. J. Phys. Chem. B *112*, 9020–9041. https://doi.org/10.1021/jp8001614.

65. Wang, J., Wang, W., Kollman, P.A., and Case, D.A. (2006). Automatic atom type and bond type perception in molecular mechanical calculations. J. Mol. Graph. Model. *25*, 247–260. https://doi.org/10.1016/j.jmgm.2005.12.005.

66. Wang, J., Wolf, R.M., Caldwell, J.W., Kollman, P.A., and Case, D.A. (2004). Development and testing of a general amber force field. J. Comput. Chem. *25*, 1157–1174. https://doi.org/10.1002/jcc.20035.

67. Frisch, M.J., Trucks, G.W., Schlegel, H.B., Scuseria, G.E., Robb, M.A., Cheeseman, J.R., Scalmani, G., Barone, V., Petersson, G.A., Nakatsuji, H., et al. (2016). Gaussian 03 Rev. E.01.

68. Bayly, C.I., Cieplak, P., Cornell, W., and Kollman, P.A. (1993). A well-behaved electrostatic potential based method using charge restraints for deriving atomic charges: the RESP model. J. Phys. Chem. *97*, 10269–10280. https://doi.org/10.1021/j100142a004.

69. Peters, M.B., Yang, Y., Wang, B., Füsti-Molnár, L., Weaver, M.N., and Merz, K.M. (2010). Structural Survey of Zinc-Containing Proteins and Development of the Zinc

AMBER Force Field (ZAFF). J. Chem. Theory Comput. *6*, 2935–2947. https://doi.org/10.1021/ct1002626.

70. Jorgensen, W.L., Chandrasekhar, J., Madura, J.D., Impey, R.W., and Klein, M.L. (1983). Comparison of simple potential functions for simulating liquid water. J. Chem. Phys. *79*, 926–935. https://doi.org/10.1063/1.445869.

71. Essmann, U., Perera, L., Berkowitz, M.L., Darden, T., Lee, H., and Pedersen, L.G. (1995). A smooth particle mesh Ewald method. J. Chem. Phys. *103*, 8577–8593. https://doi.org/10.1063/1.470117.

72. Ryckaert, J.-P., Ciccotti, G., and Berendsen, H.J.C. (1977). Numerical integration of the cartesian equations of motion of a system with constraints: molecular dynamics of n-alkanes. J. Comput. Phys. *23*, 327–341. https://doi.org/10.1016/0021-9991(77)90098-5.

73. Van Gunsteren, W.F., and Berendsen, H.J.C. (1977). Algorithms for macromolecular dynamics and constraint dynamics. Mol. Phys. *34*, 1311–1327. https://doi.org/10.1080/00268977700102571.

74. Humphrey, W., Dalke, A., and Schulten, K. (1996). VMD: Visual molecular dynamics. J. Mol. Graph. *14*, 33–38. https://doi.org/10.1016/0263-7855(96)00018-5.

75. Fukuzawa, K., Watanabe, C., Okiyama, Y., and Nakano, T. (2021). How to Perform FMO Calculation in Drug Discovery. In Recent Advances of the Fragment Molecular Orbital Method, Y. Mochizuki, S. Tanaka, and K. Fukuzawa, eds. (Springer Singapore), pp. 93–125. https://doi.org/10.1007/978-981-15-9235-5_7.

76. Mochizuki, Y., Nakano, T., Koikegami, S., Tanimori, S., Abe, Y., Nagashima, U., and Kitaura, K. (2004). A parallelized integral-direct second-order M?ller?Plesset perturbation theory method with a fragment molecular orbital scheme. Theor. Chem. Acc. *112*, 442–452. https://doi.org/10.1007/s00214-004-0602-3.

77. Mochizuki, Y., Koikegami, S., Nakano, T., Amari, S., and Kitaura, K. (2004). Large scale MP2 calculations with fragment molecular orbital scheme. Chem. Phys. Lett. *396*, 473–479. https://doi.org/10.1016/j.cplett.2004.08.082.

78. Mochizuki, Y., Nakano, T., Sakakura, K., Okiyama, Y., Watanabe, H., Kato, K., Akinaga, Y., Sato, S., Yamamoto, J., Yamashita, K., et al. (2021). The ABINIT-MP Program. In Recent Advances of the Fragment Molecular Orbital Method, Y. Mochizuki, S. Tanaka, and K. Fukuzawa, eds. (Springer Singapore), pp. 53–67. https://doi.org/10.1007/978-981-15-9235-5_4.

Supplementary Table S1: Cryo-EM data collection statistics, Related to Figure 1

	AMNV complex	PTV complex
Magnification	105,000	105,000
Voltage (kV)	300	300
Electron exposure (e^{-}/Å^{2})	49.8	50.2
Defocus range (μm)	−0.6 to −1.6	−0.6 to −1.6
Pixel size (Å)	0.83	0.83
No. of micrographs	12,466	8,102

Supplementary Table S2: Data processing and refinement statistics

	AMNV 3DFlex	AMNV HM	AMNV PM	PTV 3DFlex	PTV HM	PTV PM
Data processing						
EMDB ID	EMD-64478	EMD-64479	EMD-64480	EMD-64481	EMD-64482	EMD-64483
Symmetry imposed	C_1	C_1	C_1	C_1	C_1	C_1
Particle number	467,000	467,989	467,989	99,000	99,345	99,345
Map resolution*	3.14	2.88	2.91	3.32	3.12	3.08
Refinement						
PDB ID	9UT1	9UT3	9UT4	9UT5	9UT6	9UT7
Non-hydrogen atoms	18,986	10379	8607	18677	9514	8607
Protein residues	2436	1298	1138	2399	1195	1138
DNA residues	7	7	0	6	6	0
Zinc ion	1	1	0	1	1	0
Ligand	1	1	0	1	1	0
Model vs data CC (mask)	0.81	0.86	0.87	0.79	0.82	0.83
Mean B factor (Å^2)						
Protein	174.30	142.89	116.16	155.90	130.94	117.81
DNA	118.93	84.91		109.13	98.6	
RMS deviations						
Bond length (Å)	0.003	0.003	0.003	0.002	0.003	0.002
Bond angles (°)	0.762	0.533	0.616	0.657	0.554	0.574
Validation						
MolProbity score	1.69	1.59	1.25	1.66	1.88	1.62
Clash score	6.96	7.79	4.76	5.78	9.51	8.53
Ramachandran plot						
Favored (%)	97.89	98.52	98.85	98.06	98.56	98.41
Allowed (%)	2.11	1.48	1.15	1.94	1.44	1.59
Disallowed (%)	0	0	0	0	0	0

*FSC threshold of 0.143 was used.